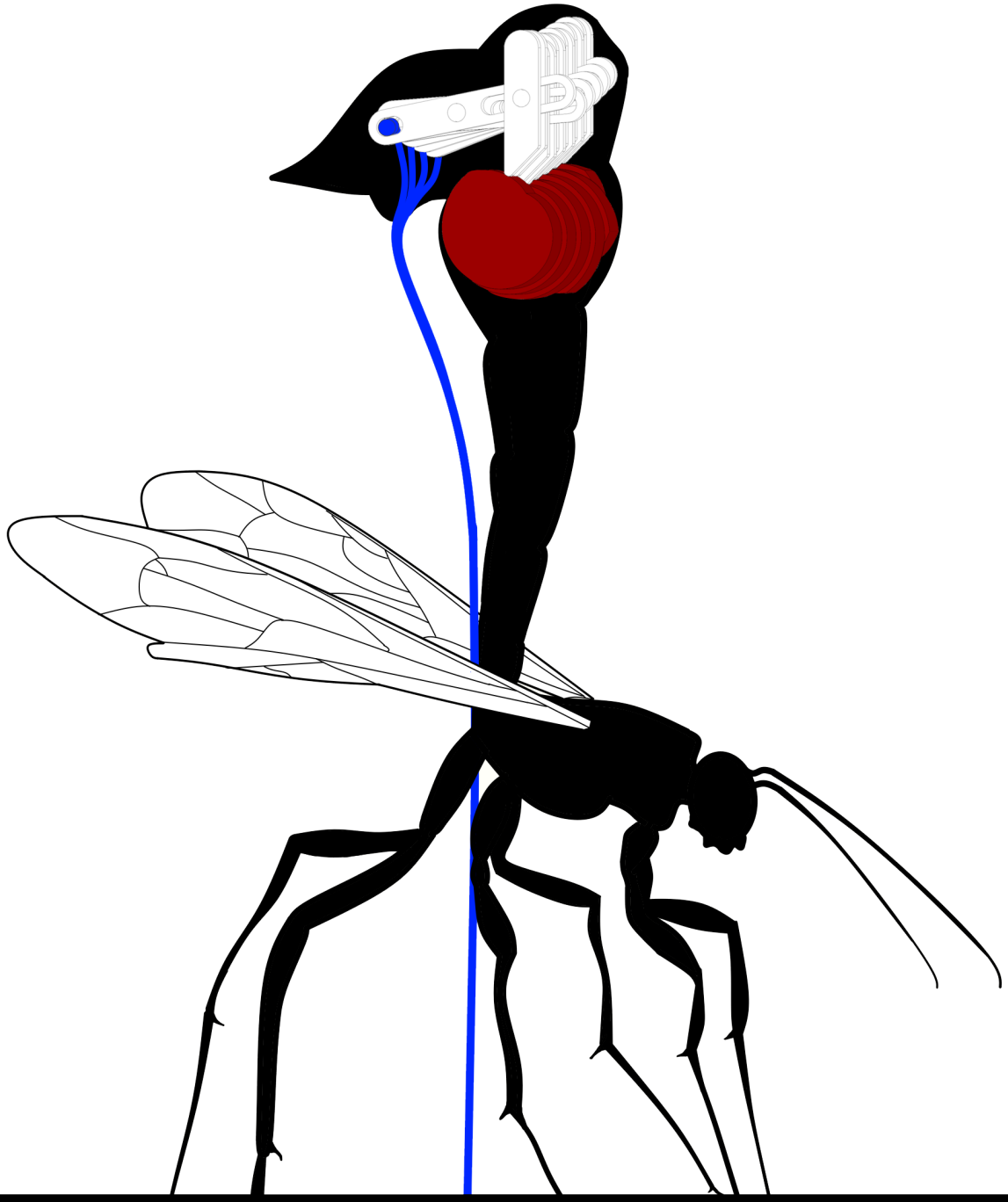

Ovipositor-Inspired Needle with Mechanical Stroke Adjustment

Jules de Ruiter

TU Delft Delft University of Technology

Ovipositor-Inspired Needle with Mechanical Stroke Adjustment

Jules de Ruiter

Student number: 4964004

In partial fulfillment of the requirements for the degree of Master of Science in Mechanical Engineering at the Delft University of Technology

Project duration: June 4 2024 - June 2 2025

Supervisors: Ir. J. Bloemberg, Ir. V. Kortman, Dr. ir. A. Sakes, Prof. dr. ir. P. Breedveeld
Thesis committee: Ir. V. Kortman, Dr. ir. T. Horeman, Prof. dr. ir. P. Breedveld

An electronic version of this thesis is available at http://repository.tudelft.nl/.

To be publically defended on June 2 2025, at 9:30.

Contents

Ovipositor-Inspired Needle with Mechanical Stroke Adjustment

Abstract

Miniaturizing needle diameter has improved patient comfort, reduced tissue damage, and lowered infection risk; however, it also increases the risk of buckling. In nature, certain wasp species have evolved slender, buckling-resistant organs known as ovipositors, which have inspired the development of bio-inspired medical needles. Despite their potential, the needle segments of ovipositor-inspired needles often suffer from high slip in *ex vivo* tissue. We hypothesize this is mainly due to connective tissue layers causing reciprocating segments to elastically deform tissue without cutting it, preventing needle propagation. To address this challenge, we established design requirements for a needle system capable of adapting to varying tissue stiffness and toughness while minimizing slip in layered tissues. Three functions were defined: transmission, stroke adjustment, and connective tissue perforation. Solutions to each were developed and integrated into concept designs. Among these, the Planar Cam Design emerged as most promising. It features a translationally symmetric cam transmission, a variable-length bar linkage for stroke adjustment, and a vibrating needle for perforating connective tissue layers. The design was fabricated and tested through two experiments: the perforation and stroke adjustment experiments, aimed at evaluating the effectiveness of the vibrating needle and the stroke control mechanism, respectively. Results from the perforation experiment suggest vibration does not significantly improve performance in layered phantom tissues. In contrast, the stroke adjustment experiment indicates that optimal stroke length varies with tissue stiffness, validating the utility of the mechanism. These findings bring ovipositor-inspired needle designs a step closer to practical clinical implementation.

1 Introduction

1.1 Background

Advancements in medical needle technology have significantly enhanced patient care by reducing discomfort, minimizing tissue damage, and improving procedural outcomes. The development of finer needles has been instrumental in achieving these benefits. For instance, smaller needle diameters and lower insertion forces have been shown to reduce the frequency of painful injections, thereby increasing patient acceptance [1]. Additionally, smaller needles minimize tissue damage, reducing both pain and the risk of infection [2].

Buckling is a major challenge in downscaling needles. While buckling outside of the tissue can be prevented using supporting telescopic tubes, simmilarly to Takahashi et al. [3], buckling within the tissue remains a challenge, especially if the needle does not travel in a straight path [4]. This buckling causes inaccurate navigation of the needle and the lateral deformation slices the surrounding tissue.

In nature, a various needle like structures employ ingenious mechanisms that prevent buckling [5]. A variety of wasps have a very thin needle-like organ, the ovipositor. For example, wasps of the species *Apocrypta pedunculosa* use their ovipositor to penetrate figs, in order to lay their eggs in the larvae of fig wasps [6]. The morphology of their ovipositor is shown in Figure 1.1. Wasps of species *Megarhyssa praecellens* posses ovipositors that they use to drill through wood in order to access larvae to lay their eggs in. Their ovipositor are approximately 40 mm long while they are only approximately 0.2 mm in diameter [7]. This is comparable to a 33 Gauge needle, which is thinner than the finest conventional hypodermic needles [1] while having the ability to propagate through wood. By adapting the mechanisms used by these insects, thinner, buckling resistant needles could be produced.

Wasp ovipositors function using a push and pull mechanism. The ovipositor consists of three parallel segments, namely the dorsal valve and two ventral valves, that are connected with tongue and groove joint, as shown in Figure 1.1 c. By protruding one valve and retracting the other two valves, the wasp propagates its ovipositor with almost no net force and a low chance of buckling. By pulling two valves with roughly the same force as the other valve is pushed with, the wasp does not have to exert a net external force [8]. Moreover, the tension in the two valves increases the rigidity of the majority of the ovipositor [7]. Only the distal end of the protruding segment is unsupported, but by keeping the unsupported length low, buckling is prevented as well. As long as the anchoring forces on the retracting valves are greater than the sum of the friction force and the cutting force of the protruding valve, the retracting valves will not move relative to the medium, and the ovipositor will propagate. By creating asymmetry at the tip of the ovipositor, the

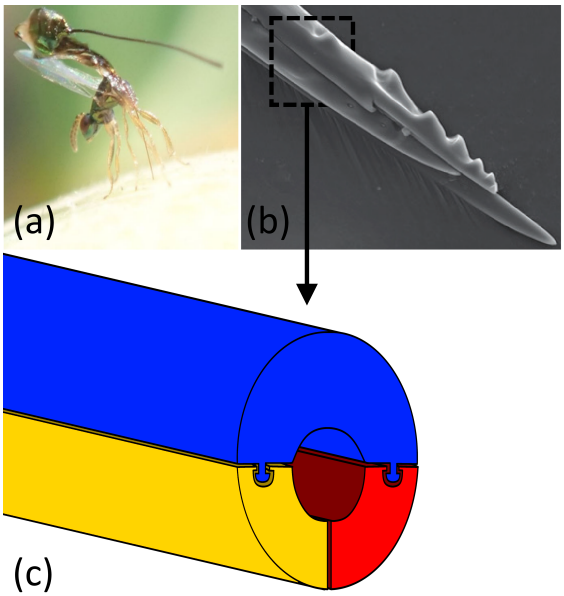

Figure 1.1: (a) A parasitic fig wasp (*Apocrypta pedunculosa*) ovipositing in a fig. Adapted from Chou et al. [9]. (b) Scanning electron micrograph of the tip of the ovipositor. The large segment at the top is the dorsal valve and the two smaller segments are the ventral valves. (c) Schematic of the cross section of the ovipositor. A tongue and groove joint connect the ventral valves (red and yellow) to the dorsal valve (blue).

wasps even have the ability to steer it [8].

A variety of ovipositor-inspired needles have been developed [10–19] that can propagate through phantoms and tissues without external force. The design used by Scali et al. [20] achieved this with a much smaller diameter than previous attempts by omitting the tongue and groove joint. The design consisted of six Nitinol wires with a diameter of 0.125 mm, held together by a PET tube at their distal ends, as shown in Figure 1.2.

The needle propagates through tissue by continually pushing forth one needle segment by a certain distance, while pulling on the other five segments, as shown in Figure 1.3. This results in a net external force of 0. From the perspective of the needle segments, the protruding needle segment move forwards by a certain distance while the other needle segments retract by $\frac{1}{5}$ that distance.

Figure 1.2: The needle systems of the designs by Scali et al. [15]. The deigns feature different needle amounts and thicknesses and are held together by PET tubes.

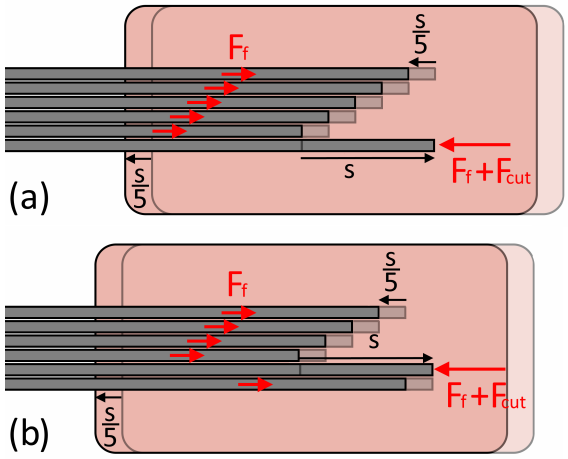

Figure 1.3: Schematic illustration of the motion and internal forces that the six needle segments experience. The protruding segment experiences a resistance of $F_f + F_{cut}$, the friction force and cutting force respectively, while the tissue exerts a force of F_f on each retracting needle segments. As long as $F_{cut} > 4F_f$, the retracting needle segments will not slip and the needle will propagate. Note that in reality, the segments are distributed hexagonally and not in one plane as pictured. (a) Between $t = 0$ and $t = T/6$, where T is the period of oscillation of each needle segment, the first segment is protruded by the stroke, s, while the other needle segments retract by $s/5$. (b) Between $t = T/6$ and $t = T/3$ the second segment is protruded, while the rest retract. When $t = T$, all six needle segments will have returned to the same relative positions as the starting position of a., but the tissue will have been pulled back by a distance of $6s/5$.

This distance shall be referred to as the stroke, s. As long as the friction between the retracting segments and the tissue is sufficient to anchor the needle, the retracting segments will remain stationary relative to the tissue and will pull it back with them. From the tissue's perspective, this results in an insertion of $\frac{s}{5}$ for the device and $\frac{6s}{5}$ for the protruding segment after $\frac{1}{6}$ of a cycle. Over the course of a full cycle, the device as a whole will have propagated by $\frac{6s}{5}$.

The protruding segment experiences a resistance consisting of the sum of the friction force and cutting force, $F_f + F_{cut}$. The tissue exerts a force of F_f on each of the 5 retracting needle segments. Therefore, as long as $F_{cut} > 4F_f$, the retracting needle segments will not slip and the needle will propagate.

A similar but thicker design by Scali et al. [15] with a diameter of 0.8 mm was tested in homogeneous phantoms, layered phantoms, and *ex vivo* tissue. The performance of the needle was defined by how much unwanted slipping occurs. When forces on the protruding segment exceeds the anchoring forces on the retracting segments, the retracting segments will no longer be stationary relative to the medium. This slipping was quantified by

defining the slip ratio, SR:

$$SR = 1 - \frac{d_{measured}}{d_{theoretical}} \quad (1)$$

Where $d_{measured}$ is the measured displacement of the needle relative to the medium and $d_{theoretical}$ is what the displacement would have been if no slip had occurred, defined by:

$$d_{theoretical} = \frac{6sn}{5} \quad (2)$$

Where s is the stroke and n are the number of cycles.

In these tests, Scali et al. [15] found that homogeneous phantoms experienced the lowest slip, layered phantoms slightly more slip, and *ex vivo* tissue significantly more slip. By identifying the underlying mechanisms for this difference, we aim to improve the design, and move closer to a clinically applicable, ovipositor-inspired needle.

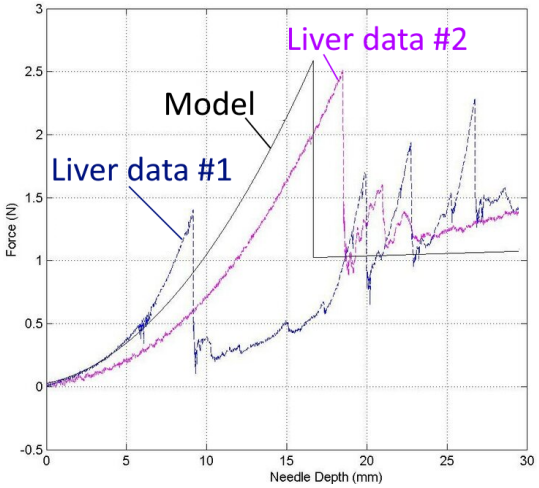

Figure 1.4: Force-insertion depth measurements (blue and pink) compared to the modeled relation. The measurements display exponential rises in force followed by abrupt drops, which Okamura et al. attribute to elastic deformation and subsequent penetration of internal structures [21].

1.2 Problem Analysis

The resistance a needle experiences during insertion in tissues is heavily influenced by the elastic deformation of connective tissue layers. In the previous Section, only the friction and cutting forces on the needle were considered. The model used by Simone and Okamura [21] in Figure 1.4 shows the elastic deformation of a liver as a spike in force, until puncture occurs, after which the force drastically drops. After this, only friction and a constant cutting force occur. The friction is a function of the surface area, which is why it is represented as a linearly increasing value as the length of the needle that is in the tissue increases. The cutting force depends only on tissue properties, which is why it is modeled as a constant value. The measurements from actual liver tissue are significantly different in value and shape. Most significantly, they show that elastic deformation cause significant spikes in penetration force, even once the needle is inside the tissue. During these elastic deformations, there is no movement of the tip of the needle relative to the tissue because the material that is in contact with the needle is being displaced as much as the needle. In this tissue, the spikes occurred approximately 2 to 4 mm apart, which the authors attribute to the encountering of interior structures.

For ovipositor-inspired needles, the lack of movement of the tip of the needle relative to the tissue could make progression through the tissue challenging. Not only does the elastic deformation cause spikes in resistance that increase the chance that slip occurs, it also causes the tissue to return to its original configuration if the needle segment moves back. Because the needle segments only reciprocate with a stroke of a few millimeters, there is a high chance that the displacement of the needle only causes elastic deformation instead of cutting. Once the segment has moved forward, it will slowly retract. If the surrounding tissue is elastically deformed, the tissue will not be pulled back with the needle segment during its retraction, but it will spring back to its undeformed shape.

Because the amount of connective tissue and its spacing varies a lot from tissue to tissue, it is important that the device can adapt in order to achieve an appropriate stroke in each tissue. In tissues with low stiffness but high toughness, a high stroke might be required in order to puncture connective tissue layers. Conversely, when the tissue is stiff, this would lead to buckling of the segments, and a low stroke would be required.

Besides slip due to elastic deformation, excessive slip due to higher resistance forces should also be addressed. By decreasing the forces on the protruding segment, or by increasing the forces acting on the retracting segments, the slip ratio could be decreased.

Ovipositor-inspired needles presented in previous studies have only operated with a predefined stroke, and have not focused on addressing the tissue stiffness forces, caused by elastic deformation of connective tissue layers. By designing mechanisms that address these issues, ovipositor-inspired needles could be brought closer to clinical application. Furthermore, by studying the efficacy of these mechanisms, our understanding of the mechanics influencing the performance of ovipositor-inspired needles could be expanded.

1.3 Goal of the Research

The goal of this study is to design and evaluate an actuation unit for the self-propelling, ovipositor-inspired needle system used by Scali et al. [20] that can adapt to the local tissue characteristics by altering its stroke during operation and perforate connective tissue layers.

1.4 Layout of the Report

Section 2 defines a set of design requirements that will result in a device that meets the goal of this study. Then, Section 3 presents functions that the device must fulfill in order to achieve the goal of this study, as well as solutions to these functions. Afterwards, Section 4 presents concept designs which consist of a combination of these solutions, and the most suitable concept design will be selected. Section 5 presents the design in more detail, along with a description of the fabrication of the prototype. Section 6 evaluates the performance of the prototype based on two experiments. Section 7 discusses the results of these experiments, the general performance of the device and the implications for the future of ovipositor-inspired needles. Finally, Section 8 presents a conclusion to this study.

2 Design Requirements

2.1 Must Haves

Must-have requirements define the core features and physical constraints that the prototype must fulfill in order to function. These specifications either directly define the functions of the device and what sets it apart from previous ovipositor-inspired needles, or are used to limit the scope of the design process. All requirements are categorized as performance- or dimension-related.

2.1.1 Performance

1. *Stroke adjustment.* The device must be able to manually adjust its stroke from 2 to 6 mm during operation, using a single input, within 10 seconds.
2. *Mechanically driven.* The device must be actuated mechanically, as electronic actuation could introduce artifacts in magnetic resonance (MR) imaging.
3. *Self-propelling motion sequence.*The device's six needle segments must be capable of executing a continuous self-propelling motion sequence, as used by Scali et al. [15] and Bloemberg [17]. Each needle segment must protrude a distance s during $\frac{1}{6}$ of its cylce at a constant speed, and retract by s during the remaining $\frac{5}{6}$ of its cycle, also at a constant speed. The segments must operate with a phase difference of 60° from each other, ensuring that at any given moment, one segment is protruding while the remaining five are retracting.
4. *Connective tissue perforation.* The device must employ a mechanism to reduce slip in phantoms emulating connective tissue layers compared to when the mechanism is not used. This phantom consists of 5 wt% gelatin with 0.5 mm thick 25 wt% gelatin layers, spaced 10 mm.

2.1.2 Dimensions

1. *Needle amount.* The device must have six parallel needle segments, as this yielded the best results for Scali et al. [15].
2. *Actuation unit length.* The length of the section of the device that drives the needle segments, the actuation unit, must be under 200 mm, to allow for handheld use in future iterations.
3. *Actuation unit diameter.* The diameter of the actuation unit must be under 80 mm, to allow for handheld use in future iterations.

2.2 Nice to Haves

Nice-to-have requirements represent desirable features that would be required for a clinically viable version of the design, but are not strictly necessary for the prototype presented in this study.

2.2.1 Performance

1. *MR compatible.* The device must be only contain materials that are MR safe according to ASTM F2503 [22]. MR Conditional materials can be used if they are tested according to the ASTM F2052 (magnetically induced force) [23], ASTM F2213 (magnetically induced torque) [24], ASTM F2182 (RF-induced heating) [25], and ASTM F2119 standards (image artifact evaluation) [26].
2. *Sterilizable.* The device shall be designed to enable validated sterilization according to the ISO 17664-1 standard [27].
3. *Biocompatible.* The materials used in the needle in contact with the patient should be biocompatible according to the ISO 10993 standard [28].
4. *Untethered.* The device must be untethered, to allow handheld use in future iterations.

2.2.2 Dimensions

1. *Needle Length.* The effective needle length must be at least 100 mm. The effective needle length is defined by the length of the needle segments that can be inserted into the tissue. This would for instance not include the telescopic tubes Scali et al. [20] used to prevent buckling of the needle segments outside of the tissue.

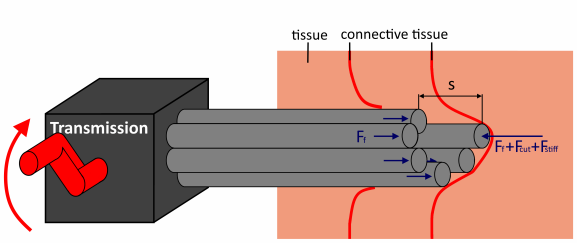

Figure 3.1: Schematic representation of the required device functions; Transmission, stroke adjustment and perforation. **Transmission:** The device must have a transmission that converts a constant rotation into the desired translation of the needle segments, represented by a black box. This motion consists of a retraction at a constant speed over $\frac{5}{6}$ of the period T, resulting in a total retraction equal to the stroke s, followed by a protrusion at a speed five times higher during the remaining $\frac{1}{6}$ of the period. The needle segments are phased 60° apart, ensuring that at any given time, one segment is protruding while the other five are retracting. **Stroke Adjustment:** The device must be able to control the stroke of the segments between 2 mm and 6 mm. The stroke of all six needle segments should be adjusted simultaneously. **Perforation:** The device must employ solutions to perforate connective tissue layers while minimizing slip. By decreasing the ratio between the force on the protruding needle segment ($F_{stiff} + F_{cut} + F_f$) and the total force acting on the retracting needle segments ($5F_f$), slip should decrease. The Figure shows the device without any solutions in place.

2. *Needle segment diameter.* The diameter of the needle segments must be 0.125 mm, as used in the W6-D0.125 needle system by Scali et al. [15].

3 Ideation Space

3.1 Functions

Three functions were defined that the device needs to fulfill in order to meet the design requirements. By combining the solutions to these functions, designs can be formed. The functions of the device are:

- **Transmission:** The device must be able to transmit a constant rotation into a complex translation, as shown in Figure 3.1 a. This translation consists of a constant backwards motion followed by a constant forwards motion that is 5 times higher than the backwards motion. The amplitude of this motion is the stroke.
- **Stroke adjustment:** The device must be able to adjust the stroke of its needle segments during operation, as illustrated in Figure 3.1 b.
- **Perforation:** The device must be able to perforate connective tissue layers while minimizing slip, as shown in Figure 3.1 c.

3.2 Solutions to Functions

3.2.1 Transmission

Cylindrical Cam

Building on the work of Sakes et al. [29], a cylindrical cam was the first transmission solution that was considered. They used a cylindrical cam rotating along the axis of the device, as shown in Figure 3.2. The cam consists of a cylinder with a groove. This groove has a constant pitch for $\frac{5}{6}$ of its circumference, and a pitch that is five times steeper and in the opposite direction for the remaining $\frac{1}{6}$. Followers are connected to pins that fit into the groove and are constrained to move exclusively along the length of the device. A schematic representation of this solution is shown in Figure 3.2 a. Alternatively, instead of using a groove, the follower can be pressed against the cam, e.g. using springs.

Planar Cam

Planar cams are another viable option. The radius of the cam should increase linearly between angles of 0 and $\frac{10\pi}{6}$ rad, corresponding to the stroke of the needle segments, and decrease over the remaining $\frac{2\pi}{6}$ rad. The follower can either be pressed against the cam, or a from fitting groove cam could be used. A schematic representation of this solution is shown in Figure 3.2 b.

Variable-Radius Gears

Variable-radius gears provide a third alternative for converting constant rotational motion into the required translational motion. When combined with a mechanism such as a Scotch-yoke to translate rotation into linear motion, these gears can achieve the desired motion, as shown in Figure 3.2 c.

The input gear consists of a top and bottom section. The top section maintains a radius r from $\theta = 0$ to $\theta = \frac{10\pi}{6}$ rad, but transitions to a slightly smaller radius from $\theta = \frac{10\pi}{6}$ rad to $\theta = 2\pi$ rad, preventing engagement with the top section of the output gear in this range. The bottom section has a radius of $\frac{5r}{3}$ between $\theta = \frac{10\pi}{6}$ rad and $\theta = 2\pi$ rad, while the remainder of its circumference has a smaller radius to prevent engagement with the bottom section of the output gear.

The output gear also has top and bottom sections. The top section maintains a radius r between $\theta = 0$ and $\theta = \pi$ rad, with a slightly smaller radius for the remaining half. The bottom section has a radius of $\frac{r}{3}$. The geometry of the input and output gears ensures that the output gear rotates at the same angular velocity as the input gear for the first $\frac{5}{6}$ of the cycle but spins five times faster during the final $\frac{1}{6}$. The Scotch-yoke then converts this rotational motion into the required translation.

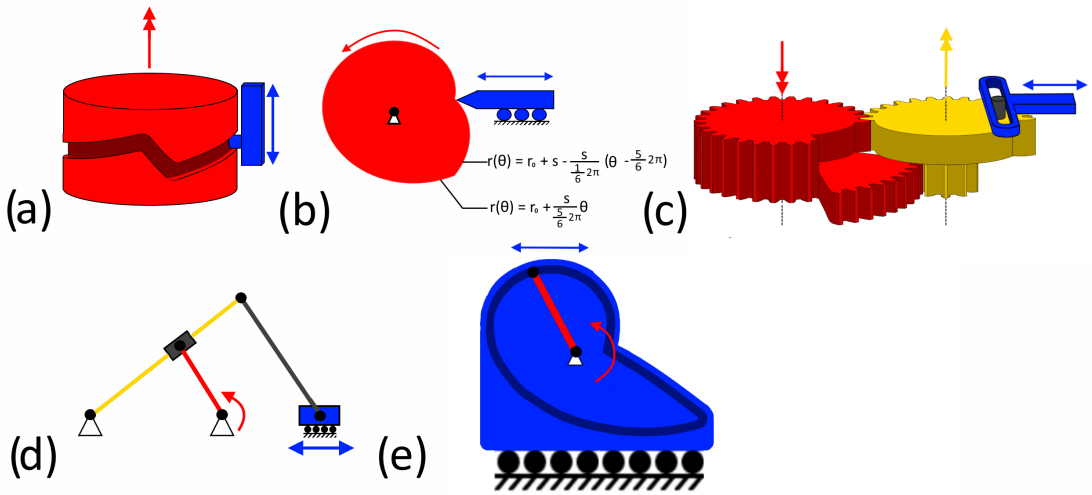

Figure 3.2: Schematic representation of the proposed transmission solutions. (a) A cylindrical cam transmission. The input rotation (red) drives a follower, which is constrained to move horizontally, producing the desired output translation (blue). (b) A planar cam transmission. (c) A variable radius gear transmission. The constant input rotation (red) is converted to a rotation that has a constant angular velocity for $\frac{5}{6}$ of the red gear's rotation, followed by an angular velocity that is 5 times higher for the remaining $\frac{1}{6}$ of the red gear's rotation. A Scotch-yoke mechanism converts this rotation into the desired translation. (d) A quick return mechanism transmission. When the end of the input crank (red) is close to the hinge of the slider link (yellow), the transmission ratio is high and the needle segment (blue) is pushed forwards quickly. When the end of the input crank on the other side, the transmission ratio is low and the needle segment is pulled backwards slowly. (e) A curved Scotch-yoke transmission. The shape of the yoke (blue) is designed to transmit the input crank's (red) constant rotation into the desired translation.

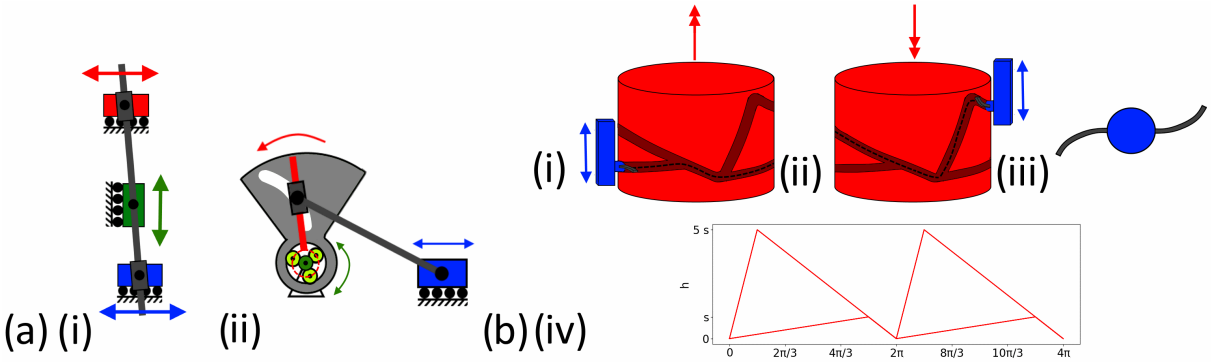

Figure 3.3: Schematic representation of the proposed stroke adjustment solutions. (a) (i) A variable-length bar linkage using translation as its input (red). Translating the adjustment slider (green) changes the distance between the input and the hinge on the adjustment slider, as well as the distance between the hinge and the output (blue), which changes the stroke. (ii) A variable-length bar linkage using constant rotation as its input (red). The adjustment knob (green) functions as the sun gear. The input crank (red) is connected to the carrier (dashed red). When the adjustment knob is rotated, the rotation is added to the input rotation through planetary gears (yellow), causing the ring gear (gray) to rotate with respect to the input crank. The ring gear is connected to the slotted disc, thus its rotation with respect to the input crank pushes the slider outward or pulls it inward. When the adjustment knob is stationary, the input crank and the slotted disc move as a single unit. (b) (i) The follower of a direction dependent cam groove rotated in the positive z direction is guided in the lower groove, resulting in a stroke of s. (ii) The follower of a direction dependent cam groove rotated in the negative z direction is guided in the upper groove, resulting in a stroke of $5s$. (iii) Side view of the follower and its steering flexures. (iv) The height of the groove h as a function of the radial coordinate θ.

Quick Return Mechanism Alternatively, a quick return mechanism could approximate the desired motion. This mechanism consists of a crank driving a slider link. The slider link connects to the needle segment via a connecting rod. When the crank nears the slider link's hinge, the transmission ratio is high, resulting in a fast forward motion. Conversely, when the crank is furthest from the hinge, the transmission ratio is low, producing a slower return motion. This solution is schematically shown in Figure 3.2 d.

Curved Scotch-Yoke Mechanism
Finally, a curved Scotch-yoke mechanism was designed to achieve the desired discontinuous output velocity. A conventional Scotch-yoke converts constant rotation into sinusoidal translation by constraining the crank end to a slot and restricting the slot's motion to perpendicular translation. The curved Scotch-yoke mechanism modifies the slot geometry to produce a more complex output motion, as shown in Figure 3.2 e. This yoke shape is derived by imposing the desired reciprocating motion on the yoke, constraining the crank to constant rotation, and tracing the crank's path on the yoke. The code used for this calculation can be found in Appendix A.

3.2.2 Stroke Adjustment

The solutions to the function of stroke adjustment can be divided into continuous and discrete stroke adjustment mechanisms. Continuous mechanisms enable any stroke length within a specified range, while discrete mechanisms allow selection among a limited number of predefined stroke lengths.

Continuous Stroke Adjustment

Continuous stroke adjustment is achieved using variable-length bar linkages. These mechanisms adjust the position of a hinge on a bar to modify the transmission ratio, enabling stroke adjustments within a continuous range. The exact design of the bar linkage depends on whether the input motion is a translation or rotation.

Figure 3.3 a. i. depicts a linkage where both the input (red) and output (blue) are linear horizontal translations. Adjusting the position of the hinge (green) vertically continuously changes the transmission ratio by altering the effective lengths between the input and the hinge and the output and the hinge.

If the input motion is rotational, and the output is translational, the adjustable hinge is in constant motion, making a simple slider impractical. A more sophisticated mechanism for adjusting the distance between two joints using rotation is described in patent US20110252909A1 [30]. This mechanism consists of an input crank with its hinge mounted on a slider, a disc with a spiral slot, and a pin that engages both the slot and the sliding hinge. As the disc rotates, the spiral slot either pushes the slider outward or pulls it inward.

Using planetary gears, the rotation of the spiral groove disc with respect to the input crank can be controlled with a single rotation of an adjustment knob that is independent of the input rotation of the slotted bar. This means that the adjustment knob is stationary when the transmission ratio is not changed, despite rotation of the slotted bar. Figure 3.3 a. ii. shows a schematic illustration of the mechanism. It consists of a ring gear that is connected to the slotted disc, an input crank connected to the planet carrier, and an adjustment knob connected to the sun gear.

Discrete stroke adjustment

Discrete stroke adjustment is achieved using a direction-dependent stroke adjustment mechanism. The user can switch between two strokes by switching the direction of the input rotation. The mechanism is designed to be combined with a transmission mechanism using a groove, such as a cam or cylindrical cam transmission. The follower is equipped with S-shaped leaf springs that press against the walls of the groove, called steering flexures (Figure 3.3 b. iii.). When combined with a cylindrical cam, the steering flexure would guide the follower into the lower path when rotated counterclockwise, and into the higher path when the cam is rotated clockwise, as shown in Figure 3.3 b. i. and b. ii.

3.2.3 Perforating Connective Tissue Layers

The solutions to the function of perforating connective tissue layers can be classified into two categories: active and passive perforation. Active perforation involves mechanisms that are actively controlled by the operator or the device, while passive perforation relies on the geometry and surface properties of the needle segments to improve perforation.

Active Perforation

The first active perforation solution revolves around initiating an extra large step with one of the needle segments on demand. When the device is trying to perforate a connective tissue layer that is too tough for the small stroke of the device to puncture, the user can manually protrude a needle segment significantly further than the stroke, perforating the connective tissue layer. In theory, the stroke adjustment mechanism could also be used to initiate the step, but this would force the range

of achievable strokes to be higher than necessary in order to achieve a minimal slip ratio. Additionally, the segment executing the large step will have a significant chance to buckle. If the step is executed through the proposed mechanism, the segment will move back and the buckling deformation will be undone. If a large step is executed using the stroke adjustment mechanism, however, the other segments will follow the buckled segment and the needle will deviate from its course.

The second active perforation solution is to add a seventh needle to the device. This perforation needle will be positioned in the middle of the six needle segments and vibrate in order to perforate connective tissue layers. Conventional needles have been shown to experience less resistance if an axial vibration is applied [31]. For ovipositor-inspired needles, it could be especially helpful since although the resistance forces are lower, the viscoelastic properties of the tissue will result in less elastic deformation of the tissue before the needle segment exerts enough force to puncture the connective tissue layer [32]. In Section 1.2, we hypothesized that the purely elastic deformation of microscopic and macroscopic connective tissue layers plays a major role in the high slip ratio Scali et al. [15] observed in tissues with more connective tissue layers, so the stiffer behavior of these tissues at higher needle velocities would reduce the slip ratio if the hypothesis is correct.

Passive Perforation

Two passive perforation solutions were identified in addition to the active solutions. The first passive solution is sharpened needle segments. This solution would decrease the cutting force, lowering the chance that the resistance force of the protracting segment is higher than the anchoring force of the retracting segments.

The second passive solution is increasing the roughness of the segments. Since the resistance of the protracting segment is equal to the cutting force and the dynamic friction force, and the anchoring force of the retracting segments is equal to the static friction force, the impact of the cutting force would decrease if both the dynamic and static friction forces increased.

3.3 Evaluation and Combination of Solutions

Each proposed solution has distinct strengths and weaknesses that influence its feasibility, performance, and compatibility with other mechanisms. Some approaches can be combined to enhance performance, while others may be mutually exclusive. The following evaluation considers the trade-offs of each solution and explores combinations that could lead to a well-integrated final design.

Evaluation of Solutions

The performance of transmission mechanisms can be assessed based on whether they produce a continuous or discontinuous output translation. With the exception of the quick-return mechanism, all proposed solutions generate a discontinuous motion, allowing for an exact realization of the desired motion. In contrast, the quick-return mechanism follows a continuous motion profile, resulting in only an approximation of the desired motion. Consequently, the retracting needle segments will not have equal velocities, leading to slip.

The performance of stroke adjustment mechanisms is primarily influenced by their range of achievable strokes and scalability. Discrete stroke adjustment mechanisms are the most compact, but are limited to a fixed set of predefined strokes, whereas continuous mechanisms offer a range of adjustable strokes. Among continuous mechanisms, those driven by rotational input require planetary gears, which pose challenges for miniaturization. Continuous mechanisms with translational input combine the benefits of adjustability and scalability.

Although the active connective tissue perforation solutions are simmilar, they have distinct advantages. The extra-large step, for example, offers reduced mechanical complexity and a lower power requirement for the device. In contrast, the vibrating perforation needle reduces both operating complexity and insertion force, even when it is not required to perforate macroscopic connective tissue layers [31].

Passive solutions offer their own set of advantages and challenges. Sharpened sections, while more effective at cutting, have the drawback of causing the needle segments to diverge due to the random orientation of the bevels. This can lead to unwanted steering of the needle and a reduced chance that a needle segment will move through a perforation made by other needle segments. Needle segments with increased roughness require higher forces for movement, which increases the likelihood of buckling occurring in the needle segments.

Combination of Solutions

The possible combinations between transmission and stroke adjustment mechanisms are limited. However, connective tissue perforation solutions are distinct in that they are not mutually exclusive, meaning a device could feature both active and passive perforation solutions.

Stroke adjustment mechanisms using variable-

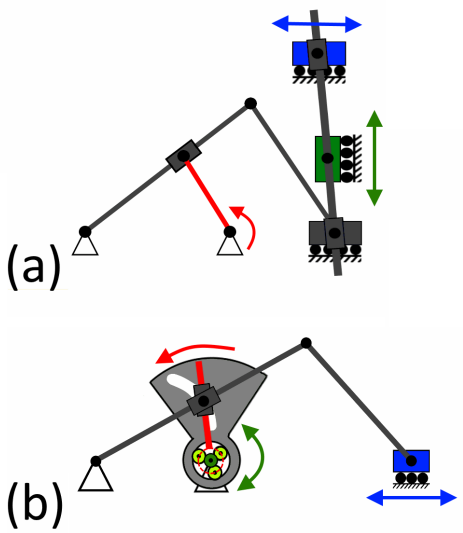

Figure 3.4: Schematic representation of how a bar linkage transmission can be combined with variable length bar mechanism stroke adjustment mechanisms that use translations (a) or rotations (b) as their input.

length bar linkages can be combined with all types of transmission mechanisms. However, the two types of stroke adjustment mechanisms proposed—those with translational input and those with rotational input—cannot always be paired with all transmission mechanisms. Cylindrical cams, planar cams, and curved Scotch-yoke mechanisms, on the other hand, can only be paired with those that use a translational input, whereas variable-radius gear and bar linkage transmissions can be combined with stroke adjustment mechanisms that use either a translational or rotational input. When paired with stroke adjustment mechanisms with a translational input, the output motion of the transmission mechanism serves as the input to the stroke adjustment mechanism. Conversely, when combined with a stroke adjustment mechanism that uses a rotational input, the output of the stroke adjustment mechanism becomes the input for the transmission mechanism. An example of this is illustrated in Figure 3.4, where a bar linkage transmission is combined with a variable-length bar linkage stroke adjustment mechanism with a translational input (a) and a rotational input (b).

Direction-dependent stroke adjustment can be combined with transmission mechanisms that use a groove, such as a curved Scotch-yoke mechanism or form-fitting cylindrical or planar cams.

4 Concept Designs

4.1 Concept Development

By combining solutions to each function, concept designs are created. Radially symmetric concept designs were the first to be conceived. In an effort to arrange the planar transmission mechanisms in a more compactly, translationally symmetric designs were then developed.

As described in Section 3.3, the chosen transmission and stroke adjustment solutions influence each other, but are not influenced by the chosen perforation solution. Therefore, the concept designs will only feature transmission and stroke adjustment solutions, and the perforation solution will be added as a separate module.

4.2 Radially Symmetric Concept Designs

4.2.1 Parallelogram Linkage Design

The first concept design uses a cylindrical cam transmission and a variable-length bar linkage stroke adjustment mechanism with a translational input. A CAD model of the concept design, along with its motion, is shown in Figure 4.1.

A drawback of this concept design is that the variable-length bar linkage stroke adjustment mechanism is more complicated than the mechanism proposed in Section 3.2.2. This is due to the fact that it is desirable that the follower and the needle segment translate in the same plane as the longitudinal axis of the device. If this is not the case, the slider link should be curved, and will not stay flush with the surface of the device when it rotates, causing unwanted moments on the pins connecting the bars and complicating the production and assembly.

4.2.2 Quick Return Design

The second concept design uses a quick return mechanism transmission and a variable-length bar linkage stroke adjustment mechanism with a rotational input. A CAD model of the concept design and a description of its motion are shown in Figure 4.2.

A drawback of this concept design is that changing the stroke does not simply scale the translation profile; it also alters its shape. The transmission already results in non-constant velocities in the protrusion phase, leading to slip, as described in Section 3.3. Pairing it with this stroke adjustment mechanism would also modify the ratio between the protrusion speed and the retraction speed, introducing additional unwanted variability to the motion.

An advantage of this concept design is that the planetary gears can be inplemented in a more integrated manner than described in Section 3.2.2. Due to the combination of this transmission mechanism and the radial symmetry of the device, only two sets of planetary gears had to be used.

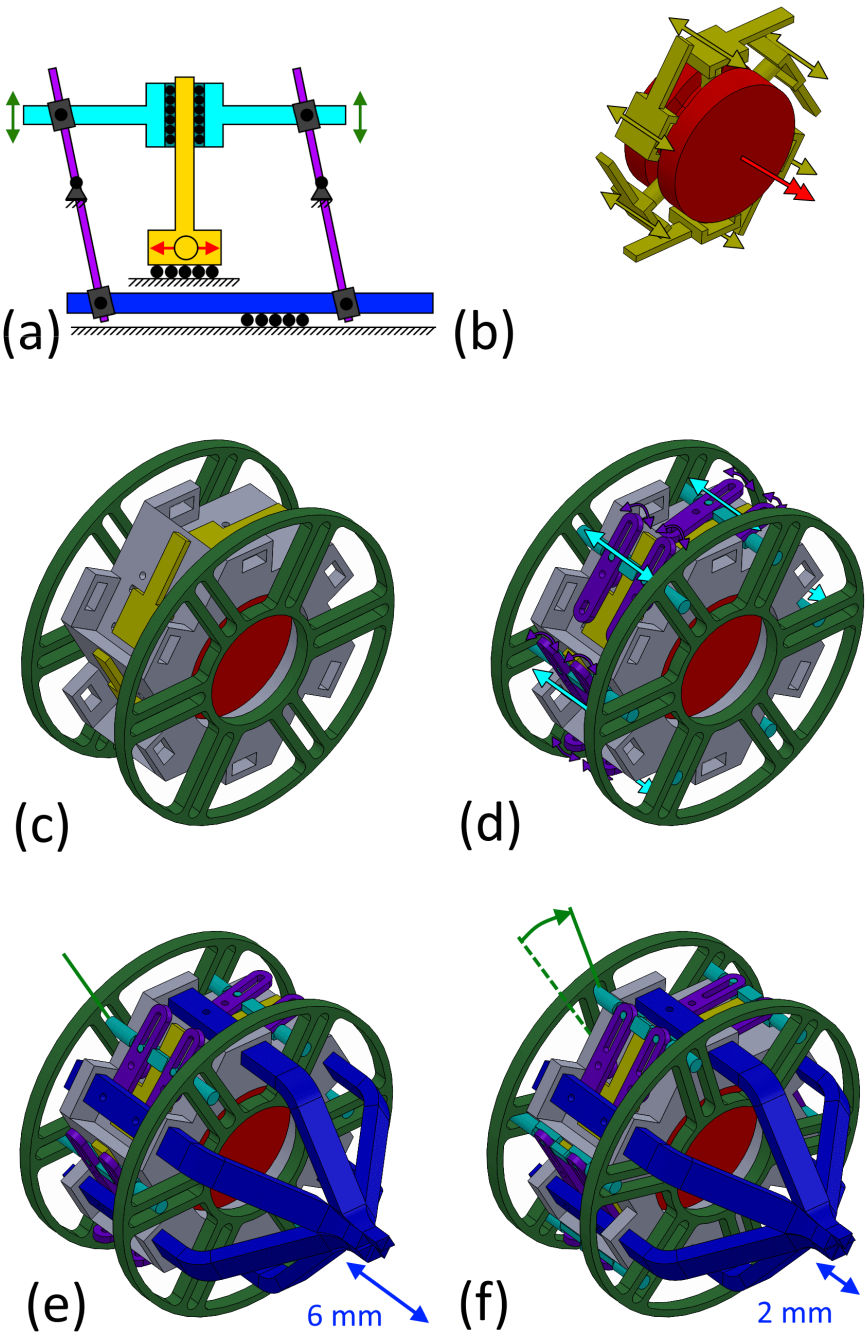

Figure 4.1: CAD model and schematic of the Parallelogram Linkage Design. (a) Schematic of the stroke adjustment mechanism driving a single segment holder. A cylindrical cam (not shown) generates the input motion (red arrow), which is transmitted to a follower (yellow). The follower and the adjustment bar (cyan) move together as a unit when the stroke is not being adjusted (green arrows). Slider bars pivot around fixed points to transmit a scaled version of the input motion to the segment holder (blue). When the adjustment wheel (not shown) is rotated, the adjustment bar slides over the follower (green arrows), adjusting the stroke. Note that in reality, the follower and the segment holder both lie in a radial plane. (b) The cylindrical cam (red) and followers (yellow). The rotation of the cam cause the followers to translate along the axis of the device, as indicated by the color coded arrows. (c) The frame (gray) and adjustment wheels (green). The frame constrains the movement of the components. The followers and segment holders (blue) are constrained to a linear translation while the cam, adjustment bracket, and slider links (purple) are constrained to one rotation. The adjustment wheels are connected, meaning they move as one. Turning them allows the user to alter the stroke. (d) The adjustment bars (cyan) and slider links. The adjustment bar and follower move as one unit as long as the adjustment wheel is stationary. This translation causes the slider link to rotate back and forth, as indicated by the color coded arrows. (e) The segment holders are connected to the slider links, transmitting their reciprocative rotation into a translation. The transmission ratio is at its highest in the pictured configuration. The pins connecting the adjustment bar to the slider link are positioned at the end of the slot closest to the hinge of the slider link, causing a larger rotation for a given translation of the adjustment bar. This results in a stroke of 6 mm. The green line indicates the position of the adjustment wheel. (f) The configuration of the device when the transmission ratio is at its lowest. The adjustment wheel is rotated from its position in d., indicated by a dashed green line, to the position indicated by the green line. This causes the adjustment bars to slide over the follower. The pins connecting the adjustment bar to the slider link are now further away from the hinge of the slider link, resulting in a lower stroke of the needle segments of 2 mm.

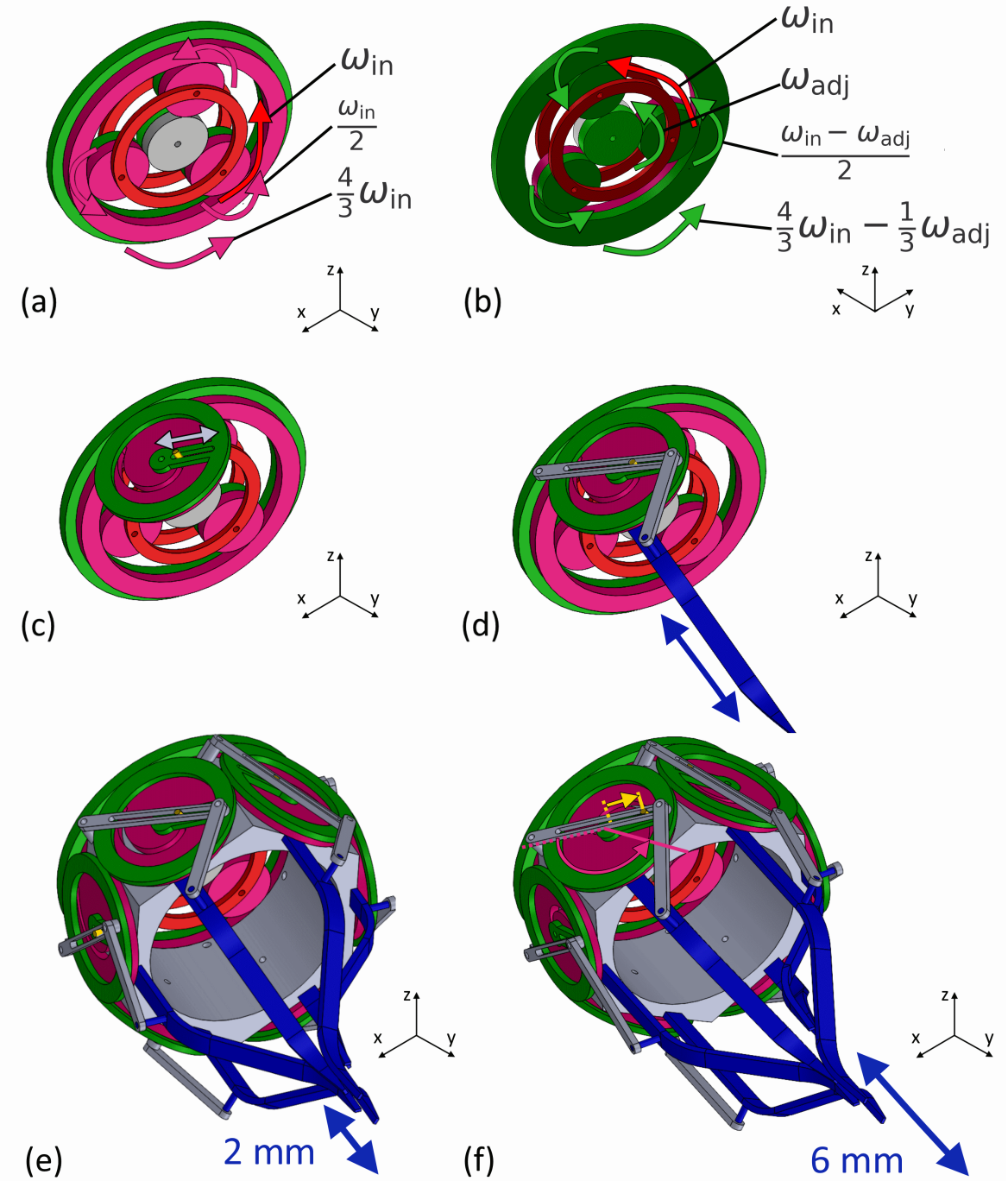

Figure 4.2: CAD model of the Quick Return Design. The device consists of two gear trains: the pink main train and the green adjustment train. (a) Isometric view of the planetary gear trains. The red carrier provides the input motion ω_{in} to both gear trains. The pink train revolves around a fixed sun gear (gray), causing the pink planetary gears to rotate with a velocity of $\frac{1}{2}\omega_{in}$, which causes the ring gear to rotate with a velocity of $\frac{4}{3}\omega_{in}$. (b) Rear isometric view of the planetary gear trains. The carrier rotates around the sun gear with a velocity of ω_{in}. The sun gear serves as the adjustment knob and rotates with a velocity of ω_{adj}. This causes the planetary gears and ring gear to rotate with velocities of $\frac{\omega_{in}-\omega_{adj}}{2}$ and $\frac{4\omega_{in}-\omega_{adj}}{3}$ respectively. This means that if the adjustment knob is not used, the two ring gears move as one unit, and if the knob is rotated, a phase difference can be induced in them. (c) The planetary gear trains and one variable-length crank, consisting of a straight-slotted disk (green) and a spiral-slotted disk (pink). When the adjustment knob is not used, the two disks move as a unit, but when it is turned, the resulting phase difference causes a pin (yellow) to be moved along the spiral slot in the pink disk by the straight slot in the green disk. (d) The planetary gear train, one variable-length crank and one quick return mechanism. The variable-length crank is connected to a slider link with the aforementioned pin. A second link connects the slider link to the segment holders (blue), which are constrained to translate along the axis of the device. The quick return mechanism converts the constant rotation of the variable-length crank into a translation of the segment holder, producing a fast forward stroke and a slower retraction. (e) The Quick Return Design in a configuration where the stroke in minimal. The pin is positioned in the end of the green slot that is closest to the hinge of the disk. (f) The Quick Return Design in a configuration where the stroke in maximal. The pin is has moved from its position in e. (yellow dashed line) to a position that is farthest away from the hinge of the disk (yellow line). This movement is caused by a rotation of the spiral-slotted disk from its position in e. (pink dashed line) to its new position (pink line).

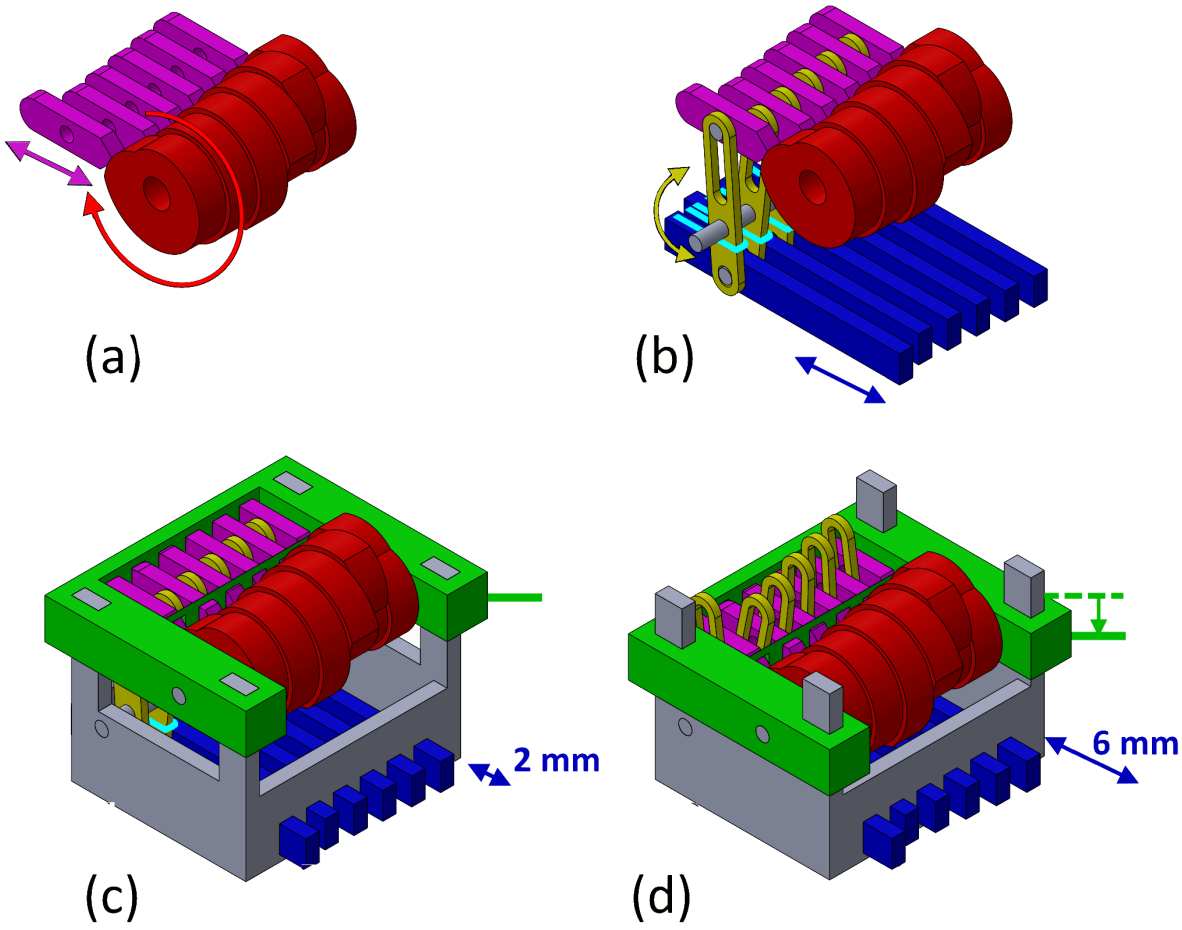

Figure 4.3: CAD model of the Planar Cam Design. (a) Six cams (red) drive followers (pink) back and forth. A constant rotation is transmitted to the desired translation. (b) The followers each cause a slider link (yellow) to rotate back and forth. This rotation drives the needle segments (blue) back and forth. Elastic cords (cyan) keep the followers pressed against the cams. (c) The Planar Cam Design in the configuration where the stroke is minimal. The Adjustment bracket (green) is at its maximal height, causing the followers to engage with the slider link at the point farthest away from the hinge of the slider link. This causes a relatively small rotation of the slider joint for a given translation of the follower. This in turn cause the needle segments to translate with a stroke of 2 mm. The green line indicates the position of the adjustment bracket. (d) The Planar Cam Design in the configuration where the stroke is maximal. The Adjustment bracket (green) is at its minimal height, causing the followers to engage with the slider link at the point closest to the hinge of the slider link. This causes a relatively large rotation of the slider joint for a given translation of the follower. This in turn cause the needle segments to translate with a stroke of 6 mm. The green line and the dashed green line indicate the position of the adjustment bracket and the position of the adjustment bracket in c. respectively.

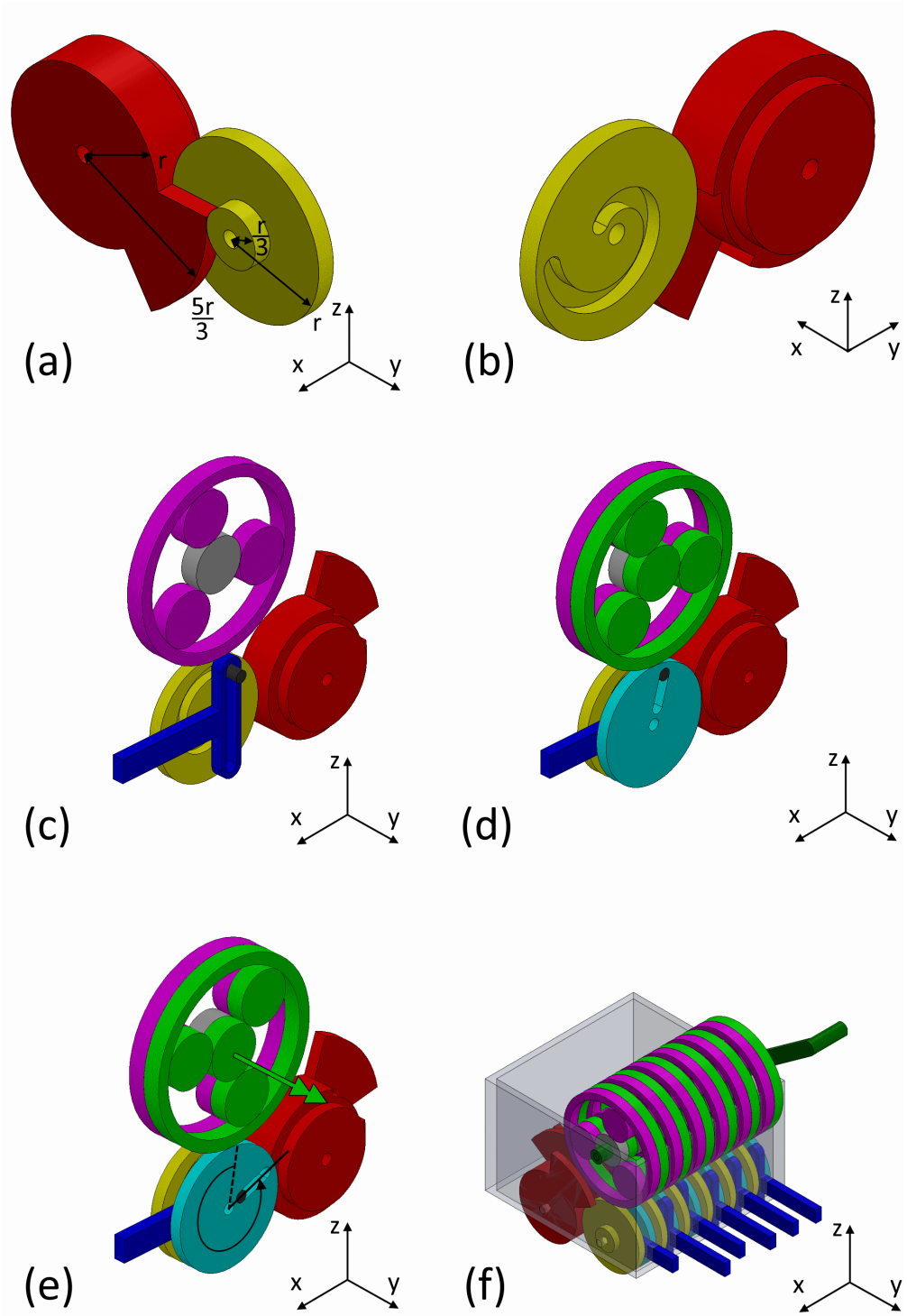

Figure 4.4: CAD model of the Variable-Radius Gear Design. (a) The input gear (red) rotates at a constant angular velocity ω. This causes the output gear (yellow) to rotate at an angular velocity of ω for half of its rotation, when the sections with a radius of r engage with each other, and with a velocity of 5ω when the sections with radii of $\frac{5r}{3}$ and $\frac{r}{3}$ engage with each other. (b) A spiral slot in the output gear is used to change the stroke. (c) A pin (black) connects a yoke (blue) to the output gear. A set of planetary gears (pink) engages with the output gear and revolves around a sun gear (gray) that is fixed to the frame. This gear train shall be referred to as the reference gear train. (d) The adjustment gear train (green) consists of a ring gear that moves freely from the reference gear train's ring gear, planetary gears that rotate freely around an axle that they share with the reference gear train's planetary gears, and a sun gear that is not connected to the the reference gear train. When the adjustment gear train's sun gear is stationary, the two gear trains move as a unit, transferring the output gear's motion to the slotted disk (cyan). This will cause it to move in unison with the output gear, meaning that the pin will stay in the same position in the spiral slot, causing the desired translation of the yokes. The reduced radius at the side of the input gear serves a relief, preventing it from engaging with the slotted disk. The stroke is maximal in the shown configuration, as as the pin is located in the distal end of the slot. (e) The configuration of the device where the stroke is minimal. The sun of the adjustment gear train is rotated (green arrow), this rotation is subtracted from the rotation of the reference gear train. This will cause a rotation of the slotted disk with regard to the output gear (black arrow), which will move the pin in the spiral groove, changing the stroke of the device. (f) Six gear trains, as shown in e., are arranged with a 60° phase difference. The sun gear of each adjustment gear train is connected to a crank (dark green). Turning the crank will cause an identical radius change to all the six gear trains, resulting in an identical stroke adjustment.

4.3 Translationally Symmetric Concept Designs

4.3.1 Planar Cam Design

The third concept design uses a planar cam transmission and a variable-length bar linkage stroke adjustment mechanism with a translational input. A CAD model of the concept design and a description of its motion are shown in Figure 4.3.

A disadvantage of this design is that the followers are not enclosed by the cam, unlike in the other models. This choice was made because the needles are not expected to encounter significant resistance during retraction, and it allows for a more compact Planar Cam Design.

An advantage of this design is the mechanical simplicity of both the stroke adjustment mechanism and the transmission. Each segment holder is driven by a minimal set of components: a cam, a follower, and an elastic cord for transmission, along with an adjustment bracket, a slider link, and a segment holder for stroke adjustment. This results in a design that is not only more compact but also likely more robust and easier to manufacture.

4.3.2 Variable-Radius Gear Design

The fourth concept design uses a variable-radius gear transmission and a variable-length bar linkage stroke adjustment mechanism with a rotational input. A CAD model of the concept design and a description of its motion are shown in Figure 4.4.

A disadvantage of this concept design is that the transmission mechanism does not lend itself well to integrating the stroke adjustment mechanism into fewer components, like it did for the Quick Return Design. Since the disk where the stroke adjustment mechanism is integrated has a non-constant angular velocity that is not in phase with the other disks, each needs their own set of planetary gears. Note that this is not because the design is translationally symmetric. A translationally symmetrical design that uses a quick return mechanism transmission would also only need two. This led to a mechanically complex design.

4.4 Concept Design Selection

The optimal design was selected based on a single quantifiable criterion: the number of components, which serves as a direct measure of mechanical complexity. Reducing the number of components achieves three key goals: improved reliability, enhanced compactness, and easier production. Fewer components reduce potential failure points, require less tight tolerances, and simplify manufacturing processes.

Each concept design was evaluated by counting its total number of components. The design with the fewest components was selected as the optimal solution, ensuring that the final concept meets the goals of reliability, compactness, and manufacturability through decreased mechanical complexity. The Parallelogram Linkage Design, Quick Return Design, Planar Cam Design and Variable-Radius Gear Design have 34, 54, 28 and 86 components respectively.

This resulted in the Planar Cam Design being chosen. Since it requires neither planetary gears such as the designs using stroke adjustment mechanisms with a rotational input, nor the complex stroke adjustment mechanism that the Parallelogram Linkage Design is required to use, it is much less complex than the other concept designs.

Perforation is achieved through a combination of a vibrating perforation needle and sharpened needle segments, as detailed in Section 3.2.3. By incorporating both active and passive perforation solutions, the design aims to reduce slip caused by connective tissue layers.

5 Final Design

5.1 Key Components

5.1.1 Actuation System

The final design is separated into two systems; the actuation system and the needle system, as shown in Figure 5.1. The actuation system drives the needle system, and is responsible for achieving all three functions; transmission, stroke adjustment and perforation. Figure 5.1. illustrates how the components are arranged. The motion is identical to the motion described in Figure 4.3. The crankshaft (salmon) is turned to rotate the cams (red). These drive followers (pink) back and forth, that are linearly constrained by the adjustment bracket (green). The retainer bracket attaches to the underside of the adjustment brackets, allowing the followers to be attached to the sliders outside of the assembly, and be easily inserted later. The followers cause the slider links (yellow) to rotate back and forth around the slider bar axle (gray), which in turn induce the desired motion in the segment holders (blue). Springs (purple) attach to the spring bar (burgundy) and pull the bottom of the slider gears backwards, keeping the followers pressed against the cams. The segment holders are held in place by a segment holder guide (gray) that is connected to the frame (gray). The vibration unit (black) actuates the perforation needle.

Technical drawings of the components in the actuation system that had to fabricated are provided in Appendix B. These components are the frame, adjustment bracket, cam, follower, slider link, segment holder guide and retainer bracket. The segment holder is not included as the freeform geometry is best understood using the CAD file included

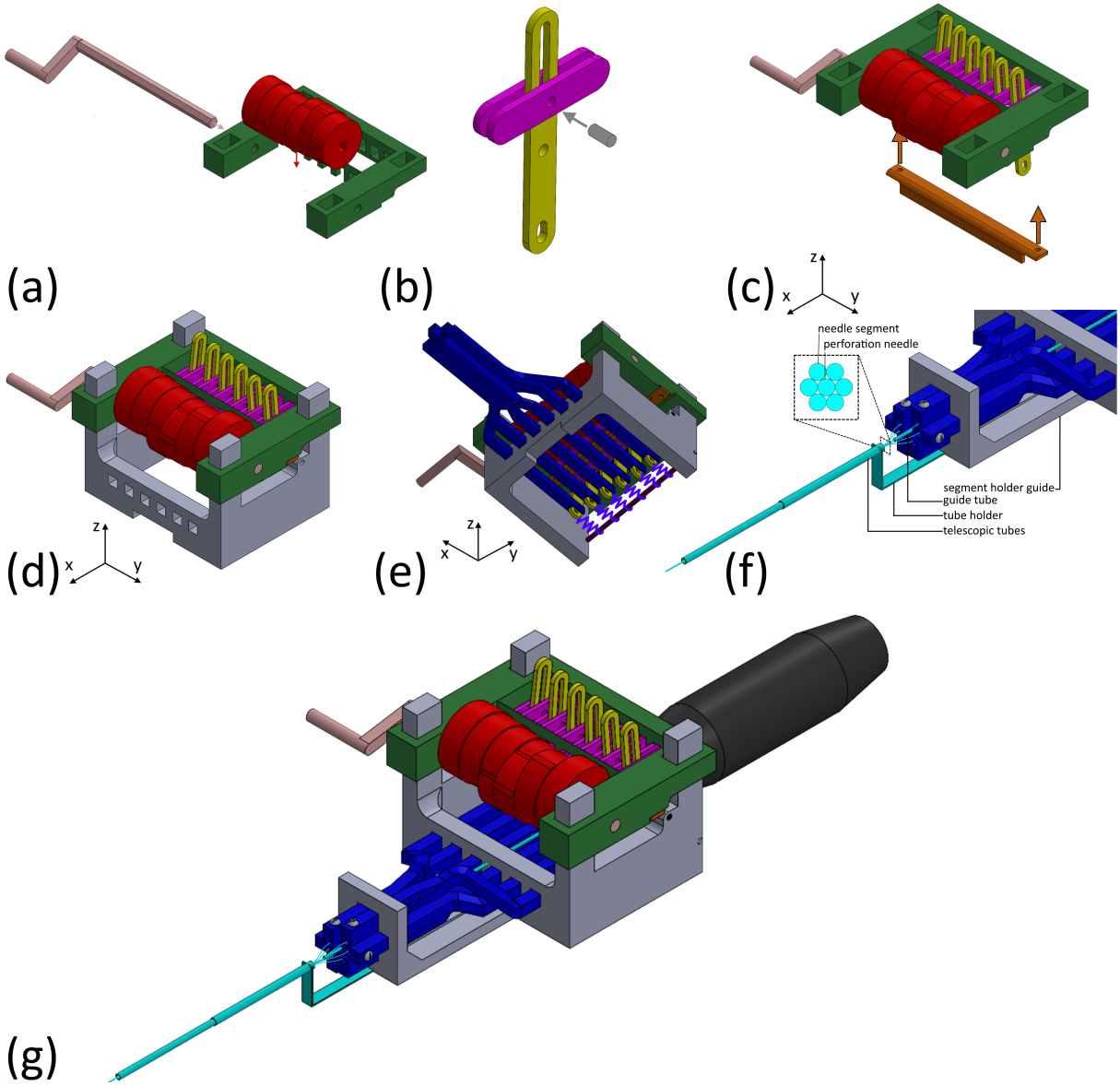

Figure 5.1: CAD model of the final design, shown in order of assembly. (a) The cams (red) are rotated 60° with regard to each other, and placed in the adjustment bracket (green). The crank (salmon) has a hexagonal cross section that fits in hexagonal holes is the cams, fixing their rotation relative to each other. (b) The followers (pink) are fixed to each other by inserting a metal rod and axially compressing the rod. The rod can slide in a groove in the slider links (yellow). (c) The slider links and followers are inserted in the adjustment bracket, and held up by the retainer bracket (orange). The followers are free to translate across the x-axis. (d) The adjustment bracket slides on the frame (gray). A friction fit allows the used to move the adjustment bracket along the y-axis. (e) The segment holders (blue) are slid through the square holes in the frame and connected to the bottom of the slider links. A tension spring (purple) connects the bottom of the slider link to the spring holder (burgundy) and keeps the followers engaged with the cams. (f) The segment holder guide (gray) is slid over the segment holders and connected to frame. The needle segments are fixed to the segment holders using M2 bolts. Buckling of the needle segments is prevented by two telescopic tubes (cyan) that are connected to the frame by the tube holder (cyan). The guide tube (cyan) prevents buckling of the perforation needle, and in inserted through the center of the segment holders, through a hole in the frame, and fixed to the spring holder. (g) The vibration unit (black) actuates the perforation needle.

in the supplementary files.

The vibration unit actuates the perforation needle with a frequency of 150 Hz and an amplitude of 1 mm. A Magi Mast tattoo machine [33] was chosen to induce the vibration. This off-the-shelf solution was selected because it meets the necessary amplitude and frequency requirements, making it suitable for assessing whether the perforation solutions improve device performance in comparison to existing alternatives. However, the device does not comply with requirements 2.1.1.2. and 2.2.1.4., as it is electromechanically driven and not untethered, as the vibration unit requires a cable. This would produce significant MR artifacts if used in practice. This limitation is acceptable for the current stage of development, as the device is intended solely to assess the efficacy of the perforation needle. In a final implementation, the vibration unit would need to be actuated using an MR compatible method.

5.1.2 Needle System

The needle system serves as the end-effector of the device. It consists of six needle segments, a perforation needle, two telescopic tubes that prevent buckling outside of tissue, the tube holder that attaches the telescopic tubes to the actuation system and a guide tube that prevents the perforation needle from buckling between the vibration unit and the telescopic tubes. At their proximal end, the needle segments are attached to the actuation system using bolts and enter the telescopic tubes. At the distal end, the needle segments are held together with a thin ring that is attached to one segment, which the other segments can slide through. The guide tube runs from the vibration unit, through a hole in the frame, through the middle of the segment holders, to the telescopic tubes. Figure 5.1 a. and d. illustrates how the components are arranged and how they connect to the actuation system respectively. The needle segments and perforation needles all have a diameter of 0.125 mm and beveled tips.

5.2 Prototype

5.2.1 Material Selection

The materials used for each component are shown in Table 1. The frame, adjustment bracket, segment holders, and holder guide were fabricated from polylactic acid (PLA) due to its suitability for rapid prototyping and the low loads these components experience. To achieve a more compact design while ensuring strength and abrasion resistance, stainless steel was selected for the followers, slider links, tube holder, slider link axle, and spring rod. Since the primary source of friction in the device was the interaction between the cams and followers, brass was chosen for the cams to optimize performance. Due to a broken electrical discharge machine, the cams were made from PLA instead of brass. The telescopic tubes, guide tube and crankshaft were made from brass, brass and stainless steel, respectively, as suitable off-the-shelf components were readily available. Nitinol was chosen for the needle segments and perforation needle due to its strength, superelasticity, biocompatibility and MR conditionality. A PET shrink tube [34] was chosen to keep the distal end of the needle system together while it moves through tissue. It was chosen due to its very low thickness and commercial availability. However, due to limited stock and long shipping times, a nylon fiber was used instead.

5.2.2 Manufacturing

The PLA components were fabricated using additive manufacturing with a Bambu Lab A1 [35] printer. The slider link axle and the spring rod were sourced from bicycle spokes with a diameter of 2.0 mm. The crankshaft was made from an M6 Allen key, as its hexagonal shape conveniently allows for the required 60° angular spacing between the cams. All other stainless steel components were laser-cut from 1.0 mm thick sheets using a Lion Alpha Metal XL [36]. The retainer plate was bent to increase its stiffness. The prototype is shown in Figure 5.3.

The needle segments were originally made from Nitinol wire [37] with a diameter of 0.125 mm. The bevel was created using electrical discharge machining and can be seen in Figure 5.2. Since the 0.125 mm thick wires were too thin to withstand the vibration, wires with a diameter of 0.25 mm [38] were selected instead. These wires were not sharpened due to a broken electrical discharge machine. The wire segments were secured to the segment holders using M2 bolts. Due to the softness of the PLA, they formed their own threads as they were driven in. To improve the bolts' grip, aluminum tubes with an inner diameter of 0.3 mm were glued to the proximal ends of the needle segments. The same was done to the perforation needle so it could be glued to the vibration unit. All glued components used the same adhesive [39].

The nylon fiber used to keep the distal end of the needle segments together was extracted from a climbing rope [40]. It was chosen due to its high strength and low thickness, of only 20 µm.

Off-the-shelf brass tubes [41] were used for the telescopic tubes and guide tube. The inner tube had an inner diameter of 0.8 mm and an outer diameter of 1.0 mm, while the outer tube had an inner diameter of 1.1 mm and an outer diameter of 1.3 mm. The guide tube had an inner diameter of 0.5 mm and an outer diameter of 0.7 mm.

Component	Material
Frame, adjustment bracket, segment holders, holder guide	PLA
Followers, slider links, tube holder, slider link axle, springs, spring rod, crankshaft	Stainless Steel
Cams*, telescopic tubes, guide tube	Brass
Needle segments, perforation needle	Nitinol
Shrink tube**	PET

Table 1: Materials used for different components. *Due to a broken electrical discharge machine, the cams were made from PLA instead. **Due to limited stock, a 20 µm nylon fiber was used instead.

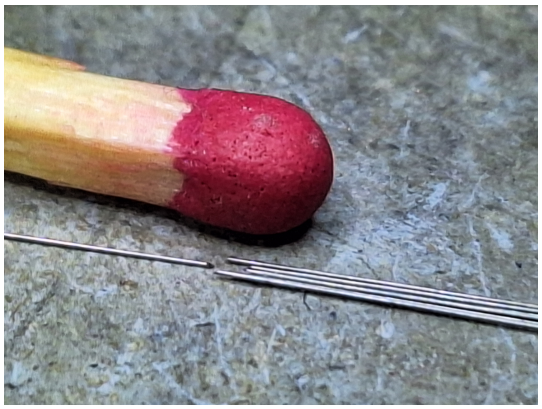

Figure 5.2: The needle segments shown with a matchstick for scale. The segments have a diameter of 0.125 mm, and the bevel is created using electrical discharge machining. The final design utilized 0.25 mm segments without a bevel.

5.2.3 Assembly

The actuation system was assembled by positioning the cams in the adjustment bracket, ensuring they were rotated 60° relative to each other. Once the hexagonal holes were aligned, the crank was inserted to secure them in place. Next, the followers were connected to the slider links. A rod was then inserted through the followers and compressed, causing radial expansion that secured the rod within the follower while allowing it to remain loose in the slider link, which had looser tolerances. The assembly was then sanded flush for a smooth fit.

The followers were inserted into the adjustment bracket and held in place by attaching the retaining bracket. The entire adjustment bracket was then slid onto the frame. The tolerances (0.3 mm) were designed to allow a friction fit where forces exerted by the user were sufficient to slide the adjustment bracket, yet it remained secure during operation.

Following this, the axle of the slider link was inserted, and the spring holder was put into place. Six springs were then attached between the spring holder and the bottom hole of the slider link. The segment holders were inserted next, and the segment holder guide was slid over them, providing a slide fit. The segment holder guide was connected to the frame with a press-fit connection. M2 bolts were driven into the segment holder to keep the needle segments in place.

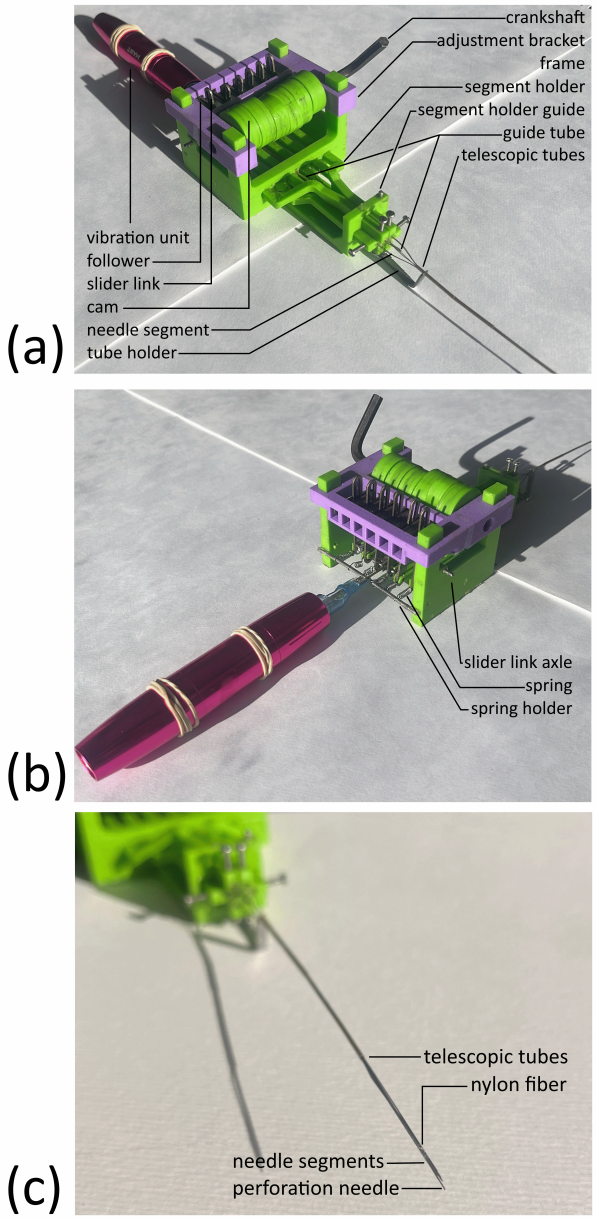

Figure 5.3: Prototype of the final design. (a) Front view of the prototype. (b) Rear view of the prototype. (c) Close-up of the distal end of the needle system.

The assembly of the needle system began with attaching the needle segments to the segment holders using bolts. Then, the guide tube was inserted through the center of the segment holders, passing through a hole in the frame. The tube rested on the spring holder and was secured in place with adhesive to the frame and the spring holder.

Next, the telescopic tubes were slid over the needle segments and connected to the tube holder using a press fit. The tube holder was glued to the segments holder using adhesive. One nylon fiber was glued to one of the needle segments, wrapped around the other segments and the perforation needle, and then tied off. The knot was secured with adhesive to prevent loosening during operation.

An aluminium tube with an inner diameter of 0.3 mm was glued to the proximal end of the perforation needle. This increased its surface area, allowing it to be securely glued to the end effector of the vibration unit - the tattoo needle.

To finalize the assembly, it was ensured that the perforation needle was situated in the center of the needle system, as shown in Figure 5.1 a. If this was not the case, the perforation needle was removed and reinserted until it properly aligned in the center.

6 Evaluation

6.1 Stroke Adjustment Experiment

6.1.1 Goal

Two experiments were conducted to assess whether the key innovations of this design — namely, the stroke adjustment mechanism and the perforation needle — enhance performance compared to previous ovipositor-inspired needles. In these experiments, performance was measured using the amount of unwanted movement of the needle segments relative to the medium, quantified as the slip ratio, as defined in Equation 1. The first experiment evaluated the impact of stroke adjustment on performance across different tissue types, while the second experiment focused on the effect of the perforation needle in layered tissues.

The stroke adjustment experiment aims to assess how stroke length affects slip in gelatin phantoms of varying stiffness. We hypothesize that there is a different trend in the relationship between stroke and slip ratio depending on the stiffness of the phantom material. This would indicate that the stroke adjustment mechanism is a valuable feature forth needle traveling through tissue layers with differing stiffnesses, since it would mean that the optimal stroke would differ depending on tissue stiffness.

6.1.2 Experimental Variables

The dependent variable in this experiment was the slip ratio, obtained by measuring the actual displacement of the phantom and comparing it to the theoretical displacement using Equation 1. A theoretical displacement of 72 mm was used for each trial. For a stroke of 2 mm, this required 30 cycles; for 4 mm, 15 cycles; and for 6 mm, 10 cycles. This The independent variables were the stroke length and gelatin concentration. The control variables were insertion depth and needle segment velocity. In order to keep these constant, the frequency of the crank was increased as the stroke decreased. By turning the crank at 1, $\frac{1}{2}$ and $\frac{1}{3}$ Hz during trials with strokes of 2, 4 and 6 mm respectively the velocities of the needle segments while the segments were retracing or protruding were kept constant between trials. Six conditions were tested, combining three stroke lengths (2, 4, and 6 mm) with two levels of phantom stiffness, resulting from gelatin concentrations of 5 wt% and 10 wt%.

6.1.3 Experimental Setup

The experimental setup of the stroke adjustment experiments is shown in Figure 6.1. On the day before the experiment, two batches of gelatin were cast in a $200 \times 160 \times 30$ mm^3 mold and refrigerated overnight. The two batches had concentrations of 5 and 10 wt% gelatin powder. On the day of the experiments, it was removed from the mold and cut into $100 \times 30 \times 30$ mm^3 blocks using a custom-made wire cutting board to ensure vertical cuts. The board, shown in Figure 6.2, features notches to secure one end of a wire [42] and holes for inserting a vertical guide. The wire runs from the notch, through the guide, to a handle, as shown in Figure 6.2. When tensioned and pulled downward, the wire ensures precise vertical cuts, even if the pulling motion is not perfectly vertical. The board consists of two laser-cut PMMA components with a thickness of 4 mm.

The phantom holder was placed on a sled on an air track [43], and the track was leveled if necessary. Placing the phantom on an air track ensures that motion of the needle through the phantom is self-propelled, with no net force. The choice was made to place the phantom on the track and keep the device stationary, because doing it the other way around introduces significant inertial forces [44] and make manual actuation unfeasible. A metronome was used to ensure the operator provided a consistent and accurate angular velocity to the crankshaft. The device was tested without a perforation needle. After the experiment, the displacement was read off the ruler on the air track.

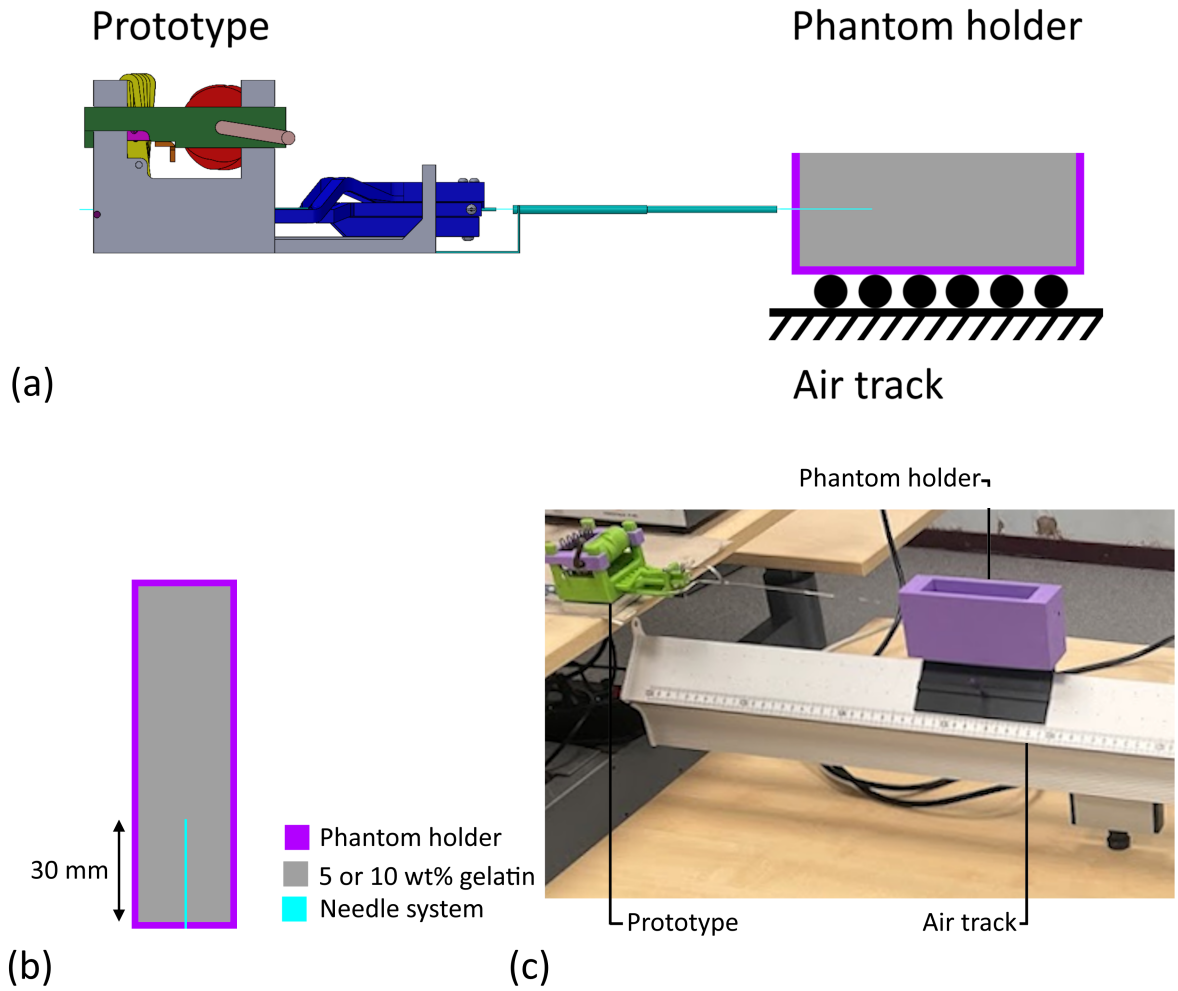

Figure 6.1: Schematic illustrations and photographs of the experimental setups used for the stroke adjustment experiments. (a) Schematic representation of the experimental setup. The crank is rotated by hand, for a specific amount of cycles, with a specific frequency. The phantom (gray) is placed in the phantom holder (purple), which slides on the air track. The displacement of the phantom holder is measured and the slip ratio is calculated. (b) Schematic top view of the phantoms in their holders. Homogeneous phantoms with concentrations of 5 or 10 wt% gelatin are used, and the needle segments have an are inserted 30 mm at the start of the experiment. (c) Photograph of the setup schematically shown in a.

6.1.4 Experimental Procedure

After the phantom was placed in the phantom holder and positioned on the sled on the air track, the needle segments were inserted 30 mm into the phantom. This was necessary because, at shallow insertion depths, the anchoring forces acting on the retracting segments are substantially lower than the resistance encountered by the protruding segment. As a result, the needle is unable to self-propel. The crank was then turned at a constant frequency until a theoretical displacement of 72 mm had occurred, calculated using Equation 2. All trials were performed on the same day.

6.1.5 Results

Figure 6.3 shows the slip ratio in phantoms of different stiffnesses at different strokes. The trend in the data seems different between the 5 and 10 wt% groups. Additionally, the variance of the results is much greater in the 5 wt% group. In a the 5 wt% phantoms, a local maximum is seen at a stroke of 4 mm, while a local minimum is seen at that stroke in 10 wt% phantoms. Furthermore, the slip ratio of the 5 wt% group remains mostly unchanged when changing the stroke from 4 to 6 mm, while the 10 wt% group experiences a notable increase. The raw data from the experiment can be found in Appendix C.

6.2 Perforation Experiment

6.2.1 Goal

The perforation experiment aims to assess the effect of the vibrating perforation needle on the device's ability to penetrate connective tissue layers while minimizing slip. It was hypothesized that the tear in the connective tissue layer made by the perforation needle would propagate when the needle segments exerted a force on the layer and that this

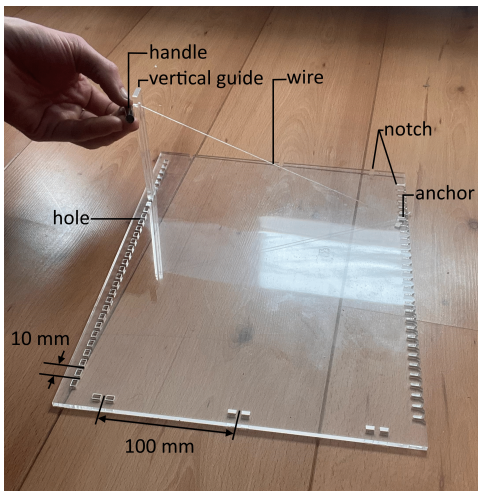

Figure 6.2: The wire cutting board enables precise and consistent cutting of gelatin blocks. Notches and holes are cut out of the board. Along the long axis of the board, these are spaced 10 mm apart, while they are spaced 100 mm along the short axis. The vertical guide can be inserted in two holes. If the wire runs from the anchor, through the notch opposite these holes, through the guide, to the handle, a consistently vertical cut can be made. The spacing of the holes and notches allows for phantoms of consistent dimensions to be cut.

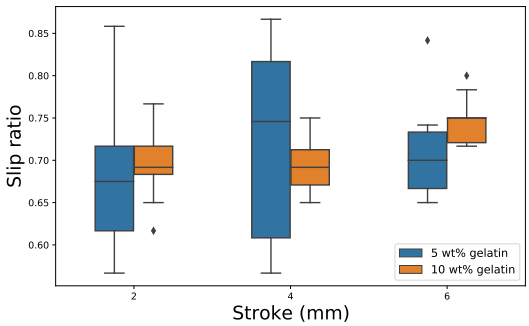

Figure 6.3: Slip ratio the device experiences for strokes of 2, 4, and 6 mm in gelatin phantoms with concentrations of 5 and 10 wt%.

force would be lower than the force required for the needle segments to penetrate the layer without prior perforation. Furthermore, the high speed of the perforation needle, combined with the viscoelastic behavior of the phantom, was hypothesized to prevent the purely elastic deformation described in Section 1.2. If confirmed, the slip ratio would be lower when using the perforation needle than when it is not in use, proving it to be a valuable feature for the device.

6.2.2 Experimental Variables

Like in the previous experiment, slip ratio was the dependent variable. The independent variable was the perforation needle presence. The control variables were stroke length, cam frequency, phantom stiffness, and initial insertion depth.

Two conditions were tested. In the first condition, the device propagated through the phantom without a perforation needle present. In the second condition, a perforation needle vibrated at a frequency of 150 Hz with an amplitude of 1 mm. In both cases, the stroke length was set to 6 mm, the needle segment frequency to 150 Hz, the gelatin concentration to 5 wt%, and the initial insertion depth to 30 mm.

6.2.3 Experimental Setup

The experimental setup of the perforation experiments is shown in Figure 6.4. On the day before the experiment, the 5 wt% gelatin was cast in a $200 \times 160 \times 30$ mm^3 mold and refrigerated overnight. On the day of the experiments, it was removed from the mold and cut into blocks of $40 \times 30 \times 30$ mm^3 and $10 \times 30 \times 30$ mm^3, using the wire cutting board described in Section 6.1.3. A batch of liquid 25 wt% gelatin was prepared. A few milliliters of liquid 25 wt% gelatin were poured onto a stainless steel sheet. A 0.5 mm thick stainless steel frame was then placed around the puddle, and pressure was applied using a third stainless steel layer. The gelatin cured within seconds, forming a 0.5 mm thick gelatin layer, from which 30×30 mm^2 sheets were cut. The sheets were prepared before each trial to prevent drying out. Each time a new sheet was made, the gelatin was reheated using a microwave. The liquid gelatin was weighed before and after heating, to compensate for evaporating water.

To assemble the layered phantom, a 40 mm long gelatin block was first placed in the phantom holder, followed by two 10 mm long blocks, and then another 40 mm long block. Gelatin sheets were inserted between each block to simulate connective tissue layers.

The phantom holder was placed on a sled on the air track. A built-in ruler was used to measure the

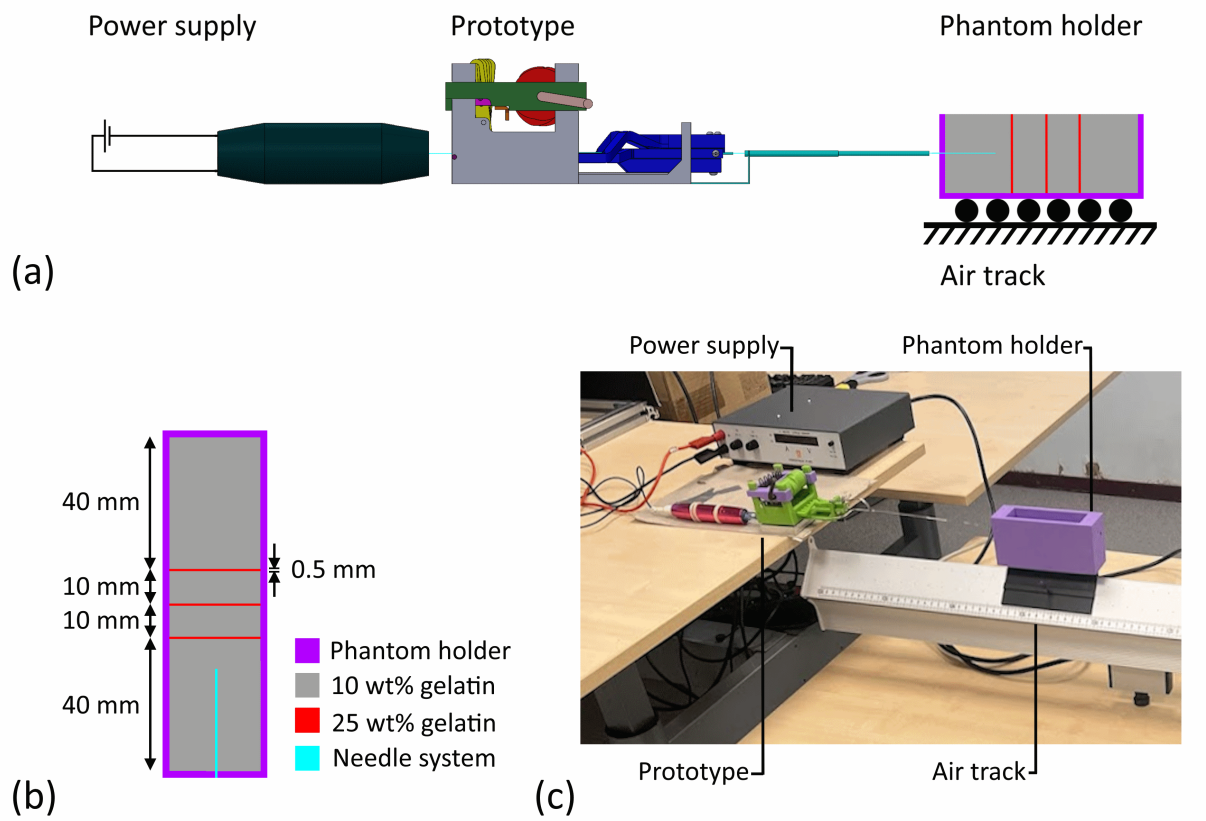

Figure 6.4: Schematic illustrations and photographs of the experimental setup used for the perforation experiments. (a) Schematic representation of the experimental setup. The power supply provides 12 V of voltage to the vibration unit, causing the perforation needle to vibrate with an amplitude of 1 mm and a frequency of 150 Hz. The crankshaft is rotated by hand, for a specific amount of cycles, with a specific frequency. The phantom (gray) is placed in the phantom holder (purple), which slides on the air track. The displacement of the phantom holder is measured and the slip ratio is calculated. (b) Schematic top view of the phantoms in their holders. The phantom consisted of 5 wt% gelatin blocks, and 25 wt% sheets. First, a 40 mm long gelatin block was placed in the phantom holder, followed by two 10 mm long blocks, and then another 40 mm long block. Gelatin sheets were inserted between each block to simulate connective tissue layers. (c) Photograph of the setup schematically shown in a.

displacement. A metronome was used to maintain a constant frequency. An adjustable power supply [45] was used to supply a 12 V voltage to the vibration unit.

6.2.4 Experimental Procedure

After the phantom was placed in the phantom holder and positioned on the sled on the air track, the needle segments were inserted 30 mm into the phantom. The crank was then turned 30 times at a frequency of 0.5 Hz. A stroke of 6 mm was used, meaning that a theoretical distance of 288 mm was traveled, as defined in Equation 2. Each condition was repeated 15 times. The phantom holder and needle segments were cleaned with water at the end of each trial. All trials were performed on the same day.

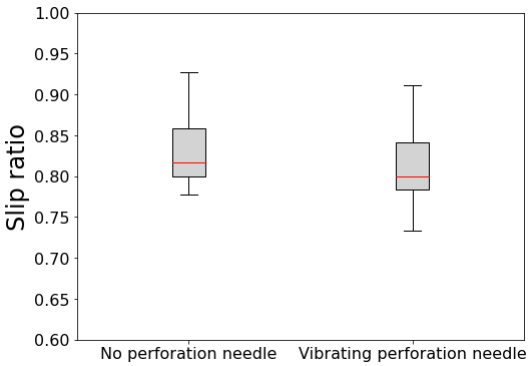

Figure 6.5: Slip the device experiences in a 5 wt% gelatin phantom with 25 wt% layers with and without a perforation needle

6.2.5 Results

As shown in Figure 6.5, a small, statistically insignificant decrease ($p = 0.201$, Welch's test) in slip ratio was observed following the addition of the perforation needle. The group without a perforation needle exhibited an average slip ratio of 0.83, compared to 0.81 in the group using a vibrating perforation needle. The raw data from the experiment can be found in Appendix C.

7 Discussion

7.1 Findings

In this study, the design process and experimental validation of a self-propelling, ovipositor-inspired needle that can adapt to different tissues by altering its stroke and perforating connective tissue layers was presented. The pneumatically actuated self-propelling, ovipositor-inspired needle presented by Hoppener et al. [19] also featured an adjustable stroke. Their design achieved this by untightening a part of the housing, moving it in line with the pistons and needle segments, and tightening it. Therefore, the stroke could not be adjusted during operation of the device, unlike the design presented in this study. Additionally, this study was the first to implement a vibrating perforation needle in the design. Another aspect where this design differentiates itself from the state of the art is the fact that it is translationally symmetric, rather than rotationally symmetric. This adjustment allowed for a significantly simpler and more compact combination of the transmission and stroke adjustment mechanism.

In the stroke adjustment experiment, the higher slip ratio observed in the 10 wt% gelatin group at a 6 mm stroke, compared with the slip ratios at strokes of 2 and 4 mm, contrasted with the absence of such an increase in the 5 wt% group, suggests that the stroke length at which the slip ratio is minimized differs based on phantom stiffness. Although the evaluated stroke range is limited, the available data indicate that optimal stroke lengths may vary with phantom stiffness. This implies that incorporating a stroke adjustment mechanism could enable the device to minimize slip across varying conditions, making it a valuable addition to the device.

In the perforation experiment, no significant difference was found in slip ratio between the groups with and without the perforation needle. This can be attributed to two factors: the unexpected toughness of the connective tissue layers and the unstable configuration of the needle segments. Firstly, the perforations made in the 25 wt% gelatin sheets did not behave as predicted. It was expected that once a small perforation was made, a tear would propagate as soon as the needle segments stretched the sheet. Instead, the needle segments struggled to penetrate the sheet, and when they did, they created new holes directly next to the hole made by the perforation needle. This issue arose across a variety of materials used to mimic connective tissue layers, including biodegradable garbage bags, plastic food wrap of varying thicknesses, plastic bags of different thicknesses, various types of paper, and wet paper. Given the range of materials tested, it is unlikely that this behavior was solely due to the high toughness of the 25 wt% gelatin and the same behaviour is expected in *in vivo* tissue.

Secondly, it was observed that the needle segments and perforation needle would often swap places during operation. This meant that one of the needle segments would not touch the phantom. This caused the anchoring force of $5F_f$, as described in Section 1.1, to be reduced to $4F_f$. This issue could have been mitigated by comparing the slip ratio of the device with a vibrating perforation needle to the slip ratio of the device with a stationary perforation needle, rather than to the device with no perforation needle. However, the current comparison is more useful in fulfilling the goal of this experiment, namely to evaluate whether the perforation needle is an improvement over existing ovipositor-inspired devices.

Given the results and underlying mechanisms, it can be concluded that there is no indication that the vibrating perforation needle improves performance or constitutes a valuable addition to the device in its current form.

7.2 Limitations

7.2.1 Prototype

Using a nylon fiber instead of the intended PET tube likely caused a significant increase in slip ratio. When the needle segment connected to the nylon fiber protruded, the phantom was observed to be pushed back, indicating slip. This spike in slip was likely not caused by the fiber's thickness itself but rather the glue securing the knots and attaching the fiber to the needle segment. The fiber was first glued to a needle segment, creating a stiff section. When the fiber was then tied around the other needle segments, this stiff section did not conform to the circumference, resulting in an excessively thick bundle. This increased thickness has been shown to increase cutting forces [21], causing more slip.

Another limitation was the occasional buckling of the needle segments between the segment holders and the telescopic tubes. This issue arises due to the lack of support of the needle segments. A potential solution to this problem would be to introduce additional support for the needle segments, similar to the approach used by Bloemberg et al. [17]. Another possibility involves directly attaching the needle segments to the bottom of the slider links, as will be discussed in Section 7.4.

7.2.2 Experiment

The primary limitation of the experiments is the small number of trials. With a larger number of trials, it would be possible to make more robust conclusions regarding the statistical significance of the results. As it stands, the current data may appear

statistically significant due to random variations in the sample, which could lead to misleading interpretations. A larger number of trials would reduce this risk and improve the reliability of the conclusions drawn from the experiments.

Another limitation is the narrow range of stroke lengths tested in the stroke adjustment experiment. Expanding the range of stroke lengths could provide an understanding of difference in the relationship between stroke and slip ratio across different phantom stiffnesses, while the current experiment merely seems to indicate that there is a difference. This broader evaluation would allow for more definitive conclusions about how the optimal stroke varies with phantom stiffness. More importantly, it would enable the identification of the optimal stroke for various phantoms, which is crucial for the design and optimization of future iterations of the device. The current range of strokes that the device is designed to achieve lacks a strong empirical basis and may not be optimal.

7.3 Towards Clinical Use

The first step towards clinical use is changing the design so that it can propagate through stationary tissue. The prototype is designed to propagate through tissue that is suspended on an air track because it ensures that there is no insertion force. Since putting the patient on a cart would be rather unpractical, the device should be placed on a cart, or the needle segment motion should change. Sprang et al. [44] placed their device on a cart and reported that the inertia and friction of the cart made interpreting their results difficult. Bloemberg et al. [46] instead altered the motion of the needle segments, which enabled the device and the patient to both remain stationary. Instead of the reciprocating motion used in this and the other studies, needle segments are protruded one by one.

Secondly, the nice-to-have requirement of sterility should be evaluated. Changing the design so that the actuation system can be sealed from contamination would mean that only the exterior of the actuation system and the needle system would need to be sterilized or replaced, eliminating the need to disassemble the device after each use. Ethylene oxide and gamma radiation sterilization are suitable techniques for the Nitinol needle segments [47], the PET shrink tube [48], and many adhesives [49] that do not cause the PET tube to shrink. A device where the needle system is sterilized separately would greatly benefit from a mechanism that enables quick removal and attachment of the needle system in a single action, rather than the current design, which requires six screws to clamp it to the actuation system. This improvement would streamline operation and provide a safer seal between the actuation system and the needle system.

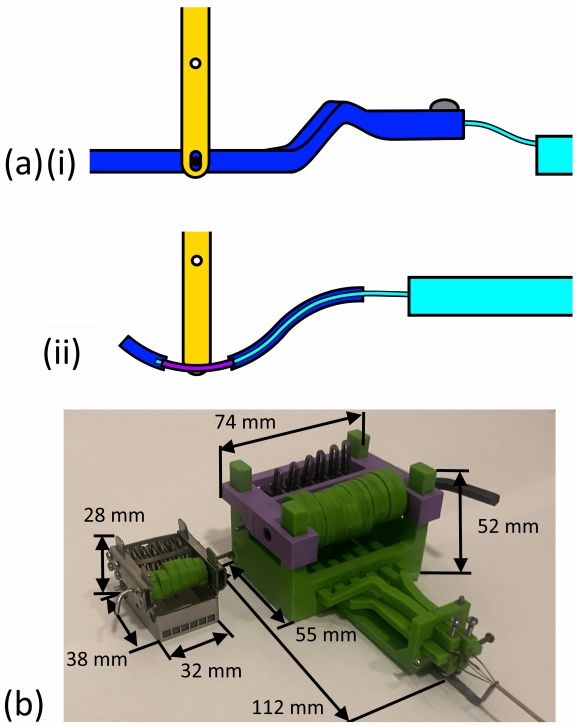

Figure 7.1: (a) (i) The current method of transmitting the rotation of the slider link (yellow) to a translation of the needle segment (cyan) requires an unsupported bend in the needle segment and a segment holder (blue) to be guided to the telescopic tube (cyan). (ii) By replacing the needle holder with a guide tube (blue) that guides a smaller tube (purple) that is fixed to the slider link, a more stable and compact design is achieved. (b) The dimensions of the prototype and the downscaled version.

Lastly, the nice-to-have requirement of MR compatibility also needs to be assessed. Magnetic Resonance Imaging (MRI) is essential for guiding the needle to its target, and therefore, the device must not pose any safety hazards or generate visual artifacts. Although all materials used in the final design are generally considered MR compatible, they may still introduce minor artifacts. The brass, stainless steel, and Nitinol may cause localized distortions in the image due to the induced currents in these conductive materials. Since the brass and stainless steel components are located outside the body, they are not expected to generate problematic distortions in the image. Note that this would require the use of a non-ferromagnetic stainless steel alloy, such as 316L stainless steel [50]. The Nitinol wire is also not expected to create significant artifacts, as Bloemberg et al. [17] successfully used an identical needle system.

7.4 Recommendations

The first improvement to the prototype should be its downscaling to enhance user-friendliness. Since the device is intended to be handheld, its current dimensions may be impractical. Reducing its size could be achieved by scaling down the cams, adjustment bracket, and frame. Additionally, replacing the segment holders with guide tubes would significantly reduce the required space. This would involve gluing metal tubes to the proximal ends of the needle segments, similar to the existing prototype. These tubes would be attached to the bottom of the slider link and designed with a bend radius equal to their distance from the slider link axle. Larger tubes would then constrain their movement and guide the needle segments toward the telescopic tubes, as illustrated in Figure 7.1 a. This modification would reduce the prototype's dimensions from $52 \times 74 \times 112$ mm^3 to $52 \times 74 \times 55$ mm^3, as shown in Figure 7.1 b.

Efforts to miniaturize the design by reducing component sizes have already been made, as demonstrated in Figure 7.1 b. By fabricating the frame and adjustment bracket from stainless steel sheet metal and halving the size of the cams, the same functionality as the original prototype can be retained while reducing the overall size to $28 \times 38 \times 32$ mm^3. However, due to the limited precision of the bent sheet metal components, the downscaled version is not yet functional.

Secondly, several fabrication improvements can enhance performance and facilitate downscaling. The prototype deviated from the final design in multiple ways, most notably the use of nylon string instead of a PET tube and the substitution of brass cams with PLA. These deviations should be addressed to ensure optimal functionality. Furthermore, if the prototype is to be downscaled, machining it from solid metal is preferable to using sheet metal, as the latter introduced precision issues that prevented it from functioning.

Thirdly, replacing the six individual cams with a single twisted cam could allow the device to accommodate an arbitrary number of needle segments. Instead of using six discrete cams, each offset by 60°, a continuous cam with a 360° helical twist along its axis could be used, as shown in Figure 7.2.

Another potential innovation that might be worth considering involves modifying the finishes or dimensions of specific needle segments. While it is uncertain whether this change would provide a clear improvement, it could address certain performance challenges. During the experiments, a spike in slip was observed when the needle segment that the ring holding together the needle segments protruded, due to the increased resistance caused by the nylon string. To counteract this, a smaller diameter for this segment could be considered. An alternative approach could involve applying a rougher surface finish to the segments that are not attached to the ring, increasing their anchoring force without adding resistance during the cutting phase. Ideally, this finish would result in a directional friction pattern, as this would increase the friction while the segments are retracting more than when they are protruding.

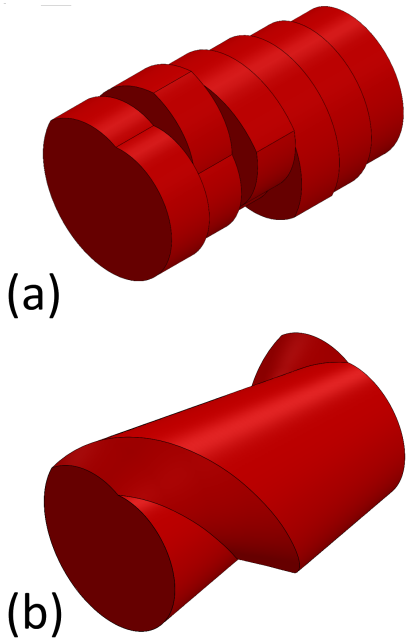

Figure 7.2: (a) The current cams, each rotated 60° relative to each other. (b) The proposed cam. Its profile is identical to the current cam's, but instead of discrete rotations, it is continually twisted.

Finally, future research should explore a wider range of stroke lengths. As discussed in Section 7.2.2, the current range lacks a strong empirical foundation. There is no study that found a conclusive optimal stroke in a given phantom, let alone optimal strokes in varying phantoms. This makes it impossible to choose a suitable range of strokes with confidence. The upper limit of viable strokes is likely constrained by the onset of needle segment buckling. In this study, no buckling was observed, suggesting that the current range does not reach this upper limit. Consequently, future experiments should investigate significantly larger strokes to better define this threshold.

The insights gained from this investigation provide a solid foundation for future design iterations, highlighting key areas for refinement and offering promising directions for enhancing the effectiveness of ovipositor-inspired needles.

8 Conclusion

This study presented the design and experimental validation of an actuation unit of a self-propelling, ovipositor-inspired needle capable of adapting to varying tissue characteristics. This began by defining a set of must-have and nice-to-have requirements, followed by the definition of three essential functions: transmission, stroke adjustment, and connective tissue perforation. Concept designs were generated by combining solutions for each function, and the most reliable, compact, and manufacturable design was selected based on component count.

The final design features a translationally symmetric cam for motion transmission, a variable-length bar linkage with translational input for stroke adjustment, and a vibrating needle to perforate connective tissue. The needle system includes six 0.25 mm Nitinol wires guided by telescopic tubes, with a seventh wire driven by a tattoo machine producing a 150 Hz, 1 mm amplitude vibration for perforation. Components were fabricated using additive manufacturing and laser cutting.

Two experiments were conducted to evaluate the design: the perforation experiment and the stroke adjustment experiment. The perforation experiment measured the slip ratio as the needle self-propelled through a layered phantom composed of 5 wt% gelatin interleaved with 0.5 mm thick 25 wt% layers. The presence of a vibrating perforation needle resulted in a small, statistically insignificant reduction in slip ratio (from 0.83 to 0.81; $p = 0.201$).

The stroke adjustment experiment investigated how stroke length and phantom stiffness affect slip ratio. Phantoms made of 5 and 10 wt% gelatin were tested with stroke lengths of 2, 4, and 6 mm. While the stroke range was limited, results suggest that optimal stroke length varies with tissue stiffness, supporting the value of a stroke adjustment mechanism.

Overall, this work advances the development of ovipositor-inspired needles by demonstrating how even mechanical devices can achieve adaptability that could improve performance in heterogeneous tissues, contributing to the pathway toward clinical application.

References

[1] HS Gill and MR Prausnitz. “Does needle size matter?” In: *Journal of diabetes science and technology* 1.5 (2007), pp. 725–729.

[2] M Loureiro et al. “Intravitreal injections of bevacizumab: the impact of needle size in intraocular pressure and pain”. In: *Journal of Current Glaucoma Practice* 11.2 (2017), p. 38.

[3] Y Takahashi et al. “Development of needle guide unit considering buckling bone-perforation control strategy based on computed tomography-guided needle insertion robot”. In: *2022 44th Annual International Conference of the IEEE Engineering in Medicine & Biology Society (EMBC)*. IEEE. 2022, pp. 4391–4396.

[4] KB Reed et al. “Robot-assisted needle steering”. In: *IEEE robotics & automation magazine* 18.4 (2011), pp. 35–46.

[5] A Sakes, D Dodou, and P Breedveld. “Buckling prevention strategies in nature as inspiration for improving percutaneous instruments: a review”. In: *Bioinspiration & biomimetics* 11.2 (2016), p. 021001.

[6] S Van Noort and A van Harten. “The species richness of fig wasps (Hymenoptera: Chalcidoidea: Agaonidae, Pteromalidae) in Yemen”. In: *Fauna of Arabia* 22 (2006), p. 449.

[7] R Wen et al. “Bending-activated biotensegrity structure enables female Megarhyssa to cross the barrier of Euler’s critical force”. In: *Science Advances* 9.42 (2023), eadi8284.

[8] U Cerkvenik et al. “Mechanisms of ovipositor insertion and steering of a parasitic wasp”. In: *Proceedings of the National Academy of Sciences* 114.37 (2017), E7822–E7831.

[9] P Chou et al. “Parasitism features of a fig wasp of genus Apocrypta (Pteromalidae: Pteromalinae) associated with a host belonging to Ficus subgenus Ficus”. In: *Insects* 14.5 (2023), p. 437.

[10] L. Frasson et al. “STING: A Soft-Tissue Intervention and Neurosurgical Guide to Access Deep Brain Lesions Through Curved Trajectories”. In: *Proceedings of the Institution of Mechanical Engineers, Part H: Journal of Engineering in Medicine* (2010).

[11] L. Frasson et al. “Experimental Evaluation of a Novel Steerable Probe with a Programmable Bevel Tip Inspired by Nature”. In: *Journal of Robotic Surgery* 6.3 (2012), pp. 189–197.

[12] A Leibinger, MJ Oldfield, and F Rodriguez y Baena. “Minimally disruptive needle insertion: a biologically inspired solution”. In: *Interface focus* 6.3 (2016), p. 20150107.

[13] M Scali et al. “Design and evaluation of a wasp-inspired steerable needle”. In: *Bioinspiration, biomimetics, and bioreplication 2017*. Vol. 10162. SPIE. 2017, pp. 34–46.

[14] V. Virdyawan, M. Oldfield, and F. R. Y. Baena. “Laser Doppler Sensing for Blood Vessel Detection with a Biologically Inspired Steerable Needle”. In: *Bioinspiration Biomimetics* 13.2 (2018), p. 026009.

[15] Marta Scali. “Self-propelling needles: From biological inspiration to percutaneous interventions”. In: (2020).

[16] TP Pusch. “From the Wasp Ovipositor to a 3D Steerable Needle for Solid-Tissue Interventions: A Design and Experimental Approach”. Master’s thesis. Delft University of Technology, 2016.

[17] J. Bloemberg. “MRI-Ready Actuation System for a Self-Propelling Needle: A Design and Experimental Approach”. Master’s thesis. Delft University of Technology, 2021.

[18] Z. Fung-A-Jou. “WASP: A Wasp-Inspired Surgery Needle for Prostate Cancer Procedures - Design and Prototyping of a Low-Friction Actuation Mechanism”. Master’s thesis. Delft University of Technology, 2023.

[19] B. Hoppener. “MRI-Compatible Pneumatic Actuation Unit for a Self-Propelling Needle”. Master’s thesis. Delft University of Technology, 2023.

[20] M Scali, P Breedveld, and D Dodou. “Experimental evaluation of a self-propelling bio-inspired needle in single-and multi-layered phantoms”. In: *Scientific reports* 9.1 (2019), p. 19988.

[21] AM Okamura, C Simone, and MD O’leary. “Force modeling for needle insertion into soft tissue”. In: *IEEE transactions on biomedical engineering* 51.10 (2004), pp. 1707–1716.

[22] ASTM International. *Standard Practice for Marking Medical Devices and Other Items for Safety in the Magnetic Resonance Environment*. https://store.astm.org/f2503-20.html. ASTM F2503-20. 2023.

[23] ASTM International. *Standard Test Method for Measurement of Magnetically Induced Displacement Force on Medical Devices in the Magnetic Resonance Environment*. https://store.astm.org/f2052-21.html. ASTM F2052-21. 2022.

[24] ASTM International. *Standard Test Method for Measurement of Magnetically Induced Torque on Medical Devices in the Magnetic Resonance Environment*. https://store.astm.org/f2213-17.html. ASTM F2213-17. 2017.

[25] ASTM International. *Standard Test Method for Measurement of Radio Frequency Induced Heating On or Near Passive Implants During Magnetic Resonance Imaging*. https://store.astm.org/f2182-19e02.html. ASTM F2182-19e2. 2019.

[26] ASTM International. *Standard Test Method for Evaluation of MR Image Artifacts from Passive Implants*. https://store.astm.org/f2119-01.html. ASTM F2119-01 (Superseded by ASTM F2119-07). 2017.

[27] International Organization for Standardization. *ISO 17664-1:2021 — Processing of health care products — Information to be provided by the medical device manufacturer for the processing of medical devices — Part 1: Critical and semi-critical medical devices*. https://www.iso.org/standard/81720.html. ISO 17664-1:2021. 2021.

[28] International Organization for Standardization. *ISO 10993-1:2018 — Biological evaluation of medical devices — Part 1: Evaluation and testing within a risk management process*. https://www.iso.org/standard/68936.html. ISO 10993-1:2018. 2018.

[29] Aimée Sakes et al. “Development of a novel wasp-inspired friction-based tissue transportation device”. In: *Frontiers in Bioengineering and Biotechnology* 8 (2020), p. 575007.

[30] Nathan Naveh, Nimrod Eitan, and Joseph Etzion. “Mechanism for changing the distance between two joints using rotation”. US20110252909A1. Oct. 2011. URL: https://patents.google.com/patent/US20110252909A1.

[31] Nikolai DM Begg and Alexander H Slocum. “Audible frequency vibration of puncture-access medical devices”. In: *Medical engineering & physics* 36.3 (2014), pp. 371–377.

[32] M Mahvash and PE Dupont. “Fast needle insertion to minimize tissue deformation and damage”. In: *2009 IEEE International Conference on Robotics and Automation*. IEEE. 2009, pp. 3097–3102.

[33] Dragonhawk. *Magi Mast [Apparatus]*. Accessed: 2025-02-26. n.d. URL: https://dragonhawkofficial.com/all-products/permanent-makeup-machines/pmu-machines/dragonhawk-tattoo-machine-rotary-pen-permanent-makeup-smp-mast-magi/.

[34] Nordson Medical. *PET Heat Shrink Tubing (103-0004)*. Retrieved March 17, 2025. n.d. URL: https://www.nordsonmedical.com/Shop/Heat-Shrink-Tubing/Products/103-0004/.

[35] Bambu Lab. *Bambu Lab A1 3D Printer*. Accessed: 2025-02-26. 2024. URL: https://bambulab.com/en-eu/a1.

[36] Lion Lasers. *Alpha Metal XL [Apparatus]*. Retrieved March 17, 2025. n.d. URL: https://lionlasers.com/en/machines/1926/.

[37] Fort Wayne Metals. *Nitinol Wire - Straight Annealed, 0.00492"*. https://www.fwmetals.com/what-we-do/materials/nitinol. Batch B200001919, Spec CD-124053-2, PO#: P2414D52600. Fort Wayne Metals, 2024.

[38] Fort Wayne Metals. *Nitinol Wire - Straight Annealed, 0.00984"*. https://www.fwmetals.com/what-we-do/materials/nitinol. Batch B200001919, Spec CD-124053-2, PO#: P2414D52600. Fort Wayne Metals, 2024.

[39] Loctite. *Super Glue Liquid Tubes*. Retrieved March 17, 2025. n.d. URL: https://www.loctiteproducts.com/products/central-pdp.html/loctite-super-glue-liquid-tubes/SAP_0201DCL029X3/variation/1399963.html.

[40] Black Diamond Equipment. *8.9 Dry Climbing Rope*. Accessed: March 12, 2025. 2025. URL: https://www.blackdiamondequipment.com/en_US/product/8-9-dry-climbing-rope/.

[41] Albion Alloys Ltd. *AA Precision Metals 2020*. Accessed: 2025-03-18. 2020. URL: https://www.albionhobbies.com/wp-content/uploads/AA-Precision-Metals-2020.pdf.

[42] Sparklin Moon. *Nylon Wire – 0.25mm*. Retrieved March 17, 2025. n.d. URL: https://www.sparklinmoon.nl/product/nylon-wire-025mm/.

[43] Eurofysica. *Luchtkussenbaan Compleet [Apparatus]*. Accessed: 2025-03-10. n.d. URL: https://www.eurofysica.nl/product/luchtkussenbaan-compleet/195050.

[44] T Sprang, P. Breedveld, and D. Dodou. "ASP-Inspired Needle Insertion with Low Net Push Force". In: *Proceedings of the 6th European Conference on Mechanism Science (EuCoMeS)*. 2016. DOI: 10.1007/978-3-319-42417-0_28.

[45] Delta Elektronika [Apparatus]. *ES 030-5 power supply*. Retrieved March 17, 2025. 2025. URL: https://www.delta-elektronika.nl/products/es150-series.

[46] J. Bloemberg et al. "Design and Evaluation of a Mechanical Pencil-Based Actuator for a Wasp-Inspired Needle". Submitted. 2025.

[47] ProPlate. *Are There Any Special Considerations for Cleaning and Sterilization of Metal-Plated Catheter-Based Components Containing Nitinol?* Retrieved March 17, 2025. n.d. URL: https://www.proplate.com/are-there-any-special-considerations-for-cleaning-and-sterilization-of-metal-plated-catheter-based-components-containing-nitinol/.

[48] Nordson Medical. *PET Heat Shrink Tubing: Technical Information*. Retrieved March 20, 2025. n.d. URL: https://www.nordsonmedical.com/Components-and-Technologies/Heat-Shrink-Tubing/PET-Heat-Shrink-Tubing/Technical-Information/.

[49] Technobis High Tech Solutions. *Adhesive Selection for Medical Devices*. Retrieved March 17, 2025. n.d. URL: https://hightechsolutions.technobis.com/blog/adhesive-selection-for-medical-devices/.

[50] A Holton et al. "Comparative mri compatibility of 316l stainless steel alloy and nickel–titanium alloy stents: Original article technical". In: *Journal of Cardiovascular Magnetic Resonance* 4.4 (2002), pp. 423–430.

Appendices

A Curved Scotch-Yoke Code

Running the following Python script will generate a plot outlining the shape of the curved Scotch-yoke. This is done by imposing a velocity v for the fist $\frac{5}{6}$ of the period, and a velocity $-5v$ for the remainder of the period on a plane, and calculating the trajectory of the end of a crank on that plane.

```
import numpy as np
import matplotlib.pyplot as plt

# Parameters
r = 4   # Radius of the crank
v=.6 # velocity of the segments during the retraction phase
omega = np.pi / 3  # Angular velocity of the crank (rad/s)
t1 = np.linspace(0, 5, 500)  # Time interval for the first motion (0 to 5 seconds)
t2 = np.linspace(5, 6, 500)  # Time interval for the second motion (5 to 6 seconds)

# Motion for 0 <= t <= 5 (positive x-direction)
x1 = v*t1 + r * np.cos(omega * t1)
y1 = r * np.sin(omega * t1)

# Motion for t > 5 (negative x-direction)
x2 = 30*v - v*5 * t2 + r * np.cos(omega * t2)
y2 = r * np.sin(omega * t2)

# Combine the paths
x = np.concatenate([x1, x2])
y = np.concatenate([y1, y2])

# Plot the path
plt.figure(figsize=(10, 6))
plt.plot(x, y)
```

B Technical Drawings Final Design

This appendix contains technical drawings of the frame, adjustment bracket, cam, retainer bracket, follower, slider link and segment holder guide. The segment holder is not included as the compound curved shape is best understood using the CAD file included in the supplementary files.

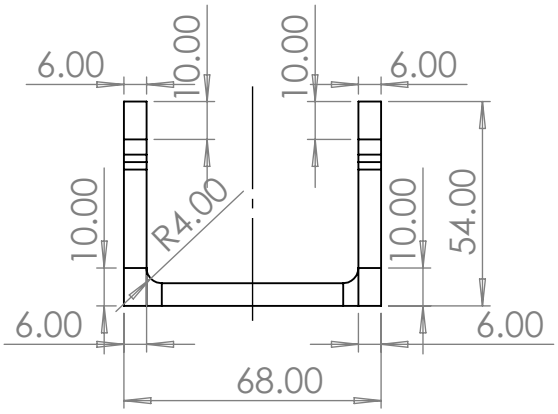

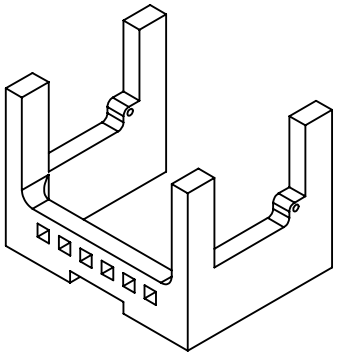

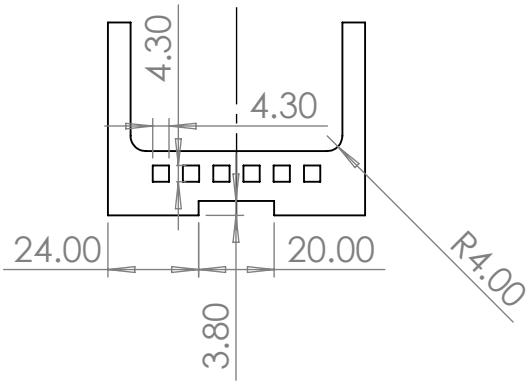

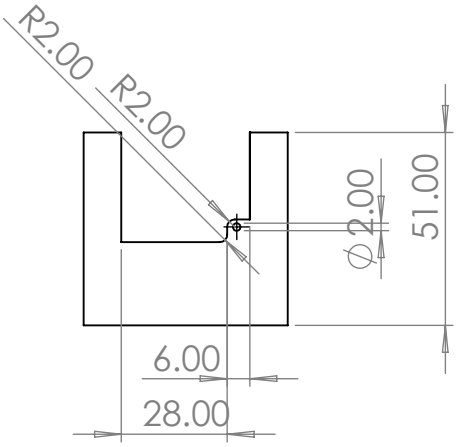

UNLESS OTHERWISE SPECIFIED: DIMENSIONS ARE IN MILLIMETERS SURFACE FINISH: TOLERANCES: LINEAR: ANGULAR:	FINISH:	DEBURR AND BREAK SHARP EDGES	DO NOT SCALE DRAWING / REVISION

	NAME	SIGNATURE	DATE
DRAWN			
CHK'D			
APPV'D			
MFG			
Q.A			

TITLE:		
MATERIAL: 32	DWG NO. frame	A4
WEIGHT:	SCALE:1:2	SHEET 1 OF 2

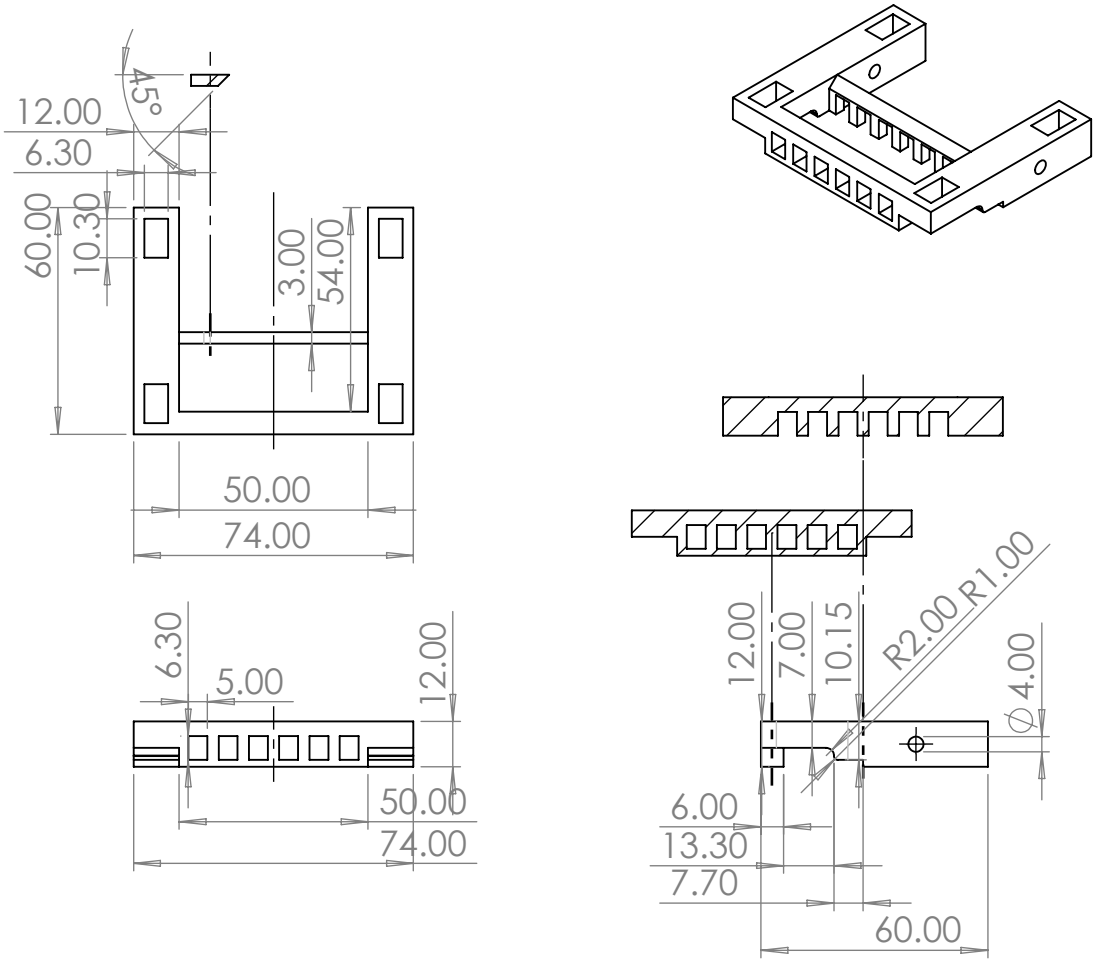

UNLESS OTHERWISE SPECIFIED: DIMENSIONS ARE IN MILLIMETERS SURFACE FINISH: TOLERANCES: LINEAR: ANGULAR:	FINISH:	DEBURR AND BREAK SHARP EDGES	DO NOT SCALE DRAWING / REVISION

	NAME	SIGNATURE	DATE
DRAWN			
CHK'D			
APPV'D			
MFG			
Q.A			

TITLE:

MATERIAL: 33

DWG NO. adjustment bracket

A4

WEIGHT:

SCALE:1:2

SHEET 1 OF 1

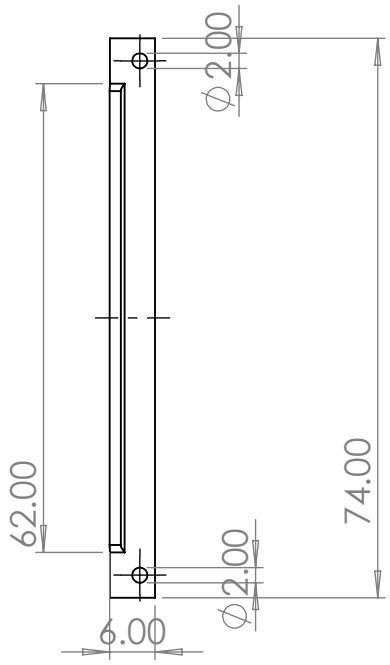

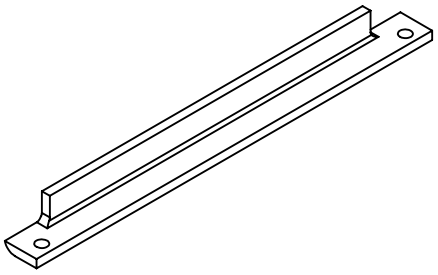

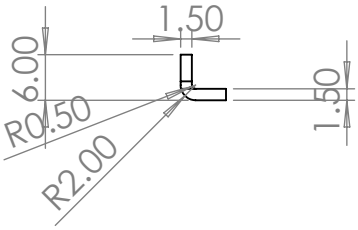

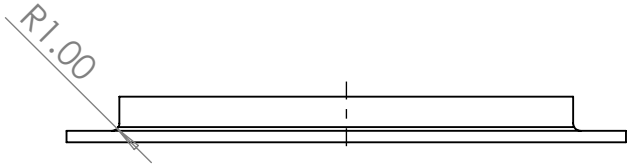

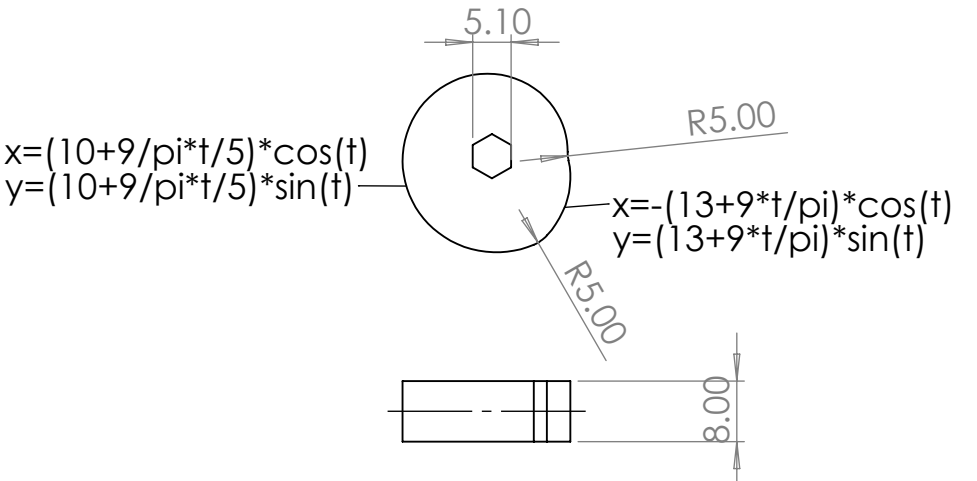

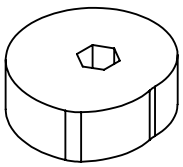

UNLESS OTHERWISE SPECIFIED: DIMENSIONS ARE IN MILLIMETERS SURFACE FINISH: TOLERANCES: LINEAR: ANGULAR:	FINISH:	DEBURR AND BREAK SHARP EDGES	DO NOT SCALE DRAWING / REVISION

	NAME	SIGNATURE	DATE
DRAWN			
CHK'D			
APPV'D			
MFG			
Q.A			

TITLE:

MATERIAL: 34

DWG NO. retainer bracket and cam

A4

WEIGHT:

SCALE:1:1

SHEET 1 OF 1

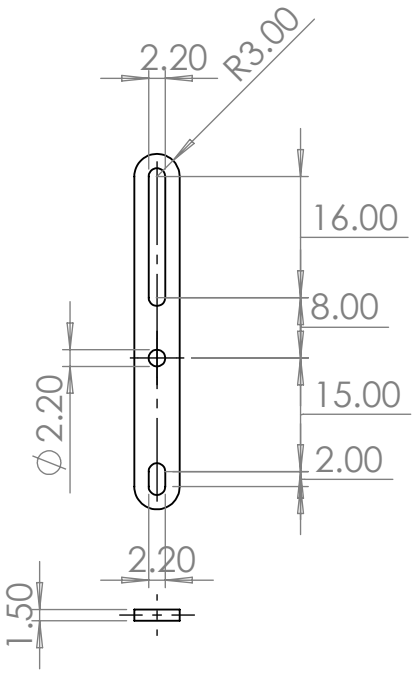

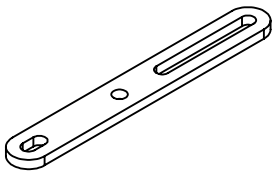

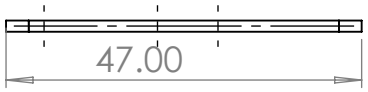

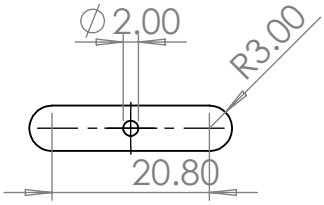

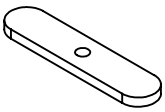

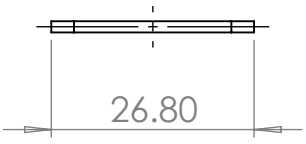

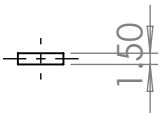

UNLESS OTHERWISE SPECIFIED: DIMENSIONS ARE IN MILLIMETERS SURFACE FINISH: TOLERANCES: LINEAR: ANGULAR:	FINISH:	DEBURR AND BREAK SHARP EDGES	DO NOT SCALE DRAWING / REVISION

	NAME	SIGNATURE	DATE
DRAWN			
CHK'D			
APPV'D			
MFG			
Q.A			

TITLE:

MATERIAL: 35

DWG NO. slider link (top) and follower (bottom)

A4

WEIGHT:

SCALE:1:1

SHEET 1 OF 1

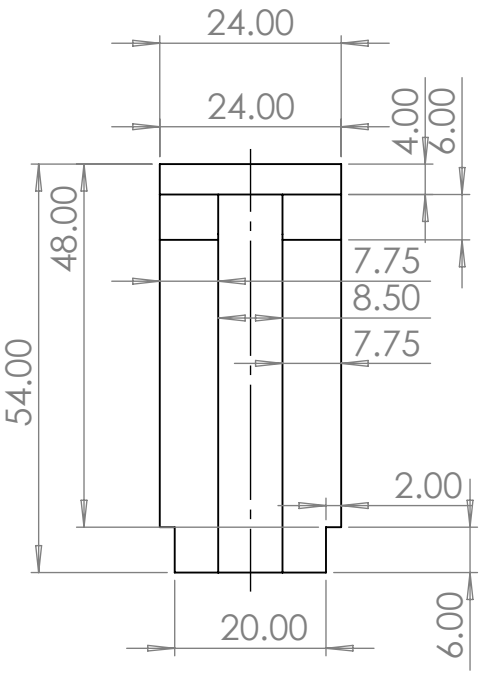

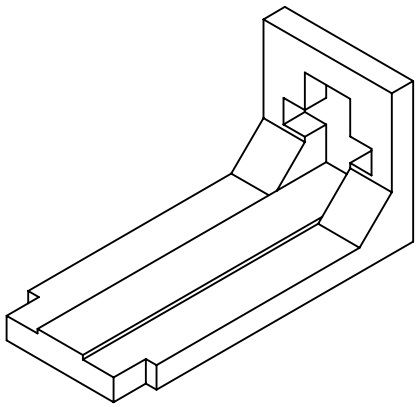

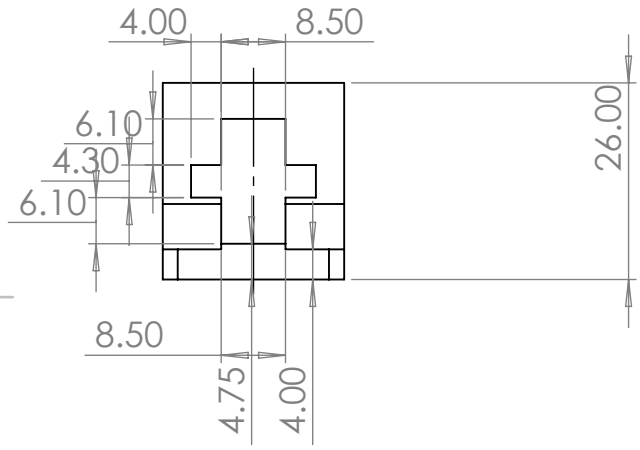

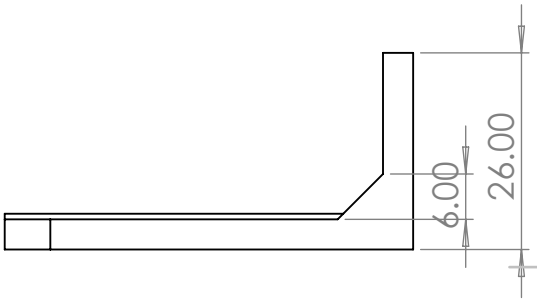

UNLESS OTHERWISE SPECIFIED: DIMENSIONS ARE IN MILLIMETERS SURFACE FINISH: TOLERANCES: LINEAR: ANGULAR:		FINISH:		DEBURR AND BREAK SHARP EDGES		DO NOT SCALE DRAWING	REVISION
	NAME	SIGNATURE	DATE			TITLE:	
DRAWN							
CHK'D							
APPV'D							
MFG							
Q.A				MATERIAL:		DWG NO.	A4
				36		segment holder guide	
				WEIGHT:		SCALE:1:1	SHEET 1 OF 1

C Raw Data Experiments

C.1 Raw Data Stroke Experiment

Table 2: Raw data of the stroke experiment

Index	Condition	Slip Ratio	Stroke	Group
1	1	0.608333	2	5 wt% gelatin
2	1	0.675000	2	5 wt% gelatin
3	1	0.858333	2	5 wt% gelatin
4	1	0.858333	2	5 wt% gelatin
5	1	0.691667	2	5 wt% gelatin
6	1	0.716667	2	5 wt% gelatin
7	1	0.616667	2	5 wt% gelatin
8	1	0.616667	2	5 wt% gelatin
9	1	0.566667	2	5 wt% gelatin
10	2	0.616667	2	10 wt% gelatin
11	2	0.766667	2	10 wt% gelatin
12	2	0.700000	2	10 wt% gelatin
13	2	0.716667	2	10 wt% gelatin
14	2	0.650000	2	10 wt% gelatin
15	2	0.683333	2	10 wt% gelatin
16	2	0.683333	2	10 wt% gelatin
17	2	0.716667	2	10 wt% gelatin
18	2	0.683333	2	10 wt% gelatin
19	2	0.750000	2	10 wt% gelatin
20	3	0.866667	4	5 wt% gelatin
21	3	0.833333	4	5 wt% gelatin
22	3	0.833333	4	5 wt% gelatin
23	3	0.741667	4	5 wt% gelatin
24	3	0.766667	4	5 wt% gelatin
25	3	0.750000	4	5 wt% gelatin
26	3	0.583333	4	5 wt% gelatin
27	3	0.583333	4	5 wt% gelatin
28	3	0.566667	4	5 wt% gelatin
29	3	0.683333	4	5 wt% gelatin
30	4	0.750000	4	10 wt% gelatin
31	4	0.666667	4	10 wt% gelatin
32	4	0.683333	4	10 wt% gelatin
33	4	0.700000	4	10 wt% gelatin
34	4	0.683333	4	10 wt% gelatin
35	4	0.700000	4	10 wt% gelatin
36	4	0.650000	4	10 wt% gelatin
37	4	0.716667	4	10 wt% gelatin
38	4	0.716667	4	10 wt% gelatin
39	4	0.666667	4	10 wt% gelatin
40	5	0.841667	6	5 wt% gelatin
41	5	0.666667	6	5 wt% gelatin
42	5	0.666667	6	5 wt% gelatin
43	5	0.708333	6	5 wt% gelatin
44	5	0.725000	6	5 wt% gelatin
45	5	0.741667	6	5 wt% gelatin
46	5	0.741667	6	5 wt% gelatin
47	5	0.700000	6	5 wt% gelatin
48	5	0.666667	6	5 wt% gelatin
49	5	0.650000	6	5 wt% gelatin

Continued on next page

Table 2: Raw data of the stroke experiment (continued)

Index	Condition	Slip Ratio	Stroke	Group
50	5	0.650000	6	5 wt% gelatin
51	6	0.750000	6	10 wt% gelatin
52	6	0.733333	6	10 wt% gelatin
53	6	0.750000	6	10 wt% gelatin
54	6	0.716667	6	10 wt% gelatin
55	6	0.783333	6	10 wt% gelatin
56	6	0.750000	6	10 wt% gelatin
57	6	0.716667	6	10 wt% gelatin
58	6	0.800000	6	10 wt% gelatin
59	6	0.716667	6	10 wt% gelatin
60	6	0.750000	6	10 wt% gelatin

C.2 Python Script for Plotting Stroke Adjustment Experiment Results

```python
import pandas as pd
import matplotlib.pyplot as plt
import seaborn as sns

# Load the dataset
slip=[0.60833333, 0.675, 0.85833333, 0.85833333, 0.69166667, 0.71666667, 0.61666667,
↪  0.61666667, 0.56666667, 0.61666667, 0.76666667, 0.7, 0.71666667, 0.65,
↪  0.68333333, 0.68333333, 0.71666667, 0.68333333, 0.75, 0.86666667, 0.83333333,
↪  0.83333333, 0.74166667, 0.76666667, 0.75, 0.58333333, 0.58333333, 0.56666667,
↪  0.68333333, 0.75, 0.66666667, 0.68333333, 0.7, 0.68333333, 0.7, 0.65,
↪  0.71666667, 0.71666667, 0.66666667, 0.84166667, 0.66666667, 0.66666667,
↪  0.70833333, 0.725, 0.74166667, 0.74166667, 0.7, 0.66666667, 0.65, 0.65, 0.75,
↪  0.73333333, 0.75, 0.71666667, 0.78333333, 0.75, 0.71666667, 0.8, 0.71666667,
↪  0.75]
condition=[1, 1, 1, 1, 1, 1, 1, 1, 1, 2, 2, 2, 2, 2, 2, 2, 2, 2, 3, 3, 3, 3, 3,
↪  3, 3, 3, 3, 4, 4, 4, 4, 4, 4, 4, 4, 4, 4, 5, 5, 5, 5, 5, 5, 5, 5, 5, 5, 6,
↪  6, 6, 6, 6, 6, 6, 6, 6]
df = pd.DataFrame({'condition': condition,
    'Slip': slip})
# Add 'Stroke' and 'Group' column based on condition
stroke_mapping = {1: 2, 3: 4, 5: 6, 2: 2, 4: 4, 6: 6}
df["Stroke"] = df["condition"].map(stroke_mapping)
df["Group"] = df["condition"].apply(lambda x: "5 wt% gelatin" if x in [1, 3, 5] else
↪  "10 wt% gelatin")

# Create boxplot
plt.figure(figsize=(8, 5))
sns.boxplot(
    data=df,
    x="Stroke",
    y="Slip",
    hue="Group",
    width=.5
)

plt.grid(False)
plt.xlabel("Stroke (mm)", size=20)
plt.ylabel("Slip ratio", size=20)
plt.legend(title="", fontsize=12)
plt.tight_layout()
plt.savefig("stroke_results.pdf", format="pdf", bbox_inches="tight")
plt.show()
```

C.3 Raw Data Perforation Experiment

Table 3: Raw data of the perforation experiment.

Index	Slip Ratio	Vibrating Perforation Needle
1	0.8667	absent
2	0.8167	absent
3	0.9278	absent
4	0.8500	absent
5	0.8056	absent
6	0.8389	absent
7	0.8222	absent
8	0.9000	absent
9	0.8111	absent
10	0.8000	absent
11	0.7778	absent
12	0.8000	absent
13	0.7778	absent
14	0.8000	absent
15	0.9222	absent
16	0.7444	present
17	0.8000	present
18	0.8444	present
19	0.8000	present
20	0.9111	present
21	0.8333	present
22	0.8556	present
23	0.8000	present
24	0.8389	present
25	0.7889	present
26	0.7333	present
27	0.7778	present
28	0.7556	present
29	0.8667	present
30	0.8167	present

C.4 Python Script for Plotting Perforation Experiment Results

```python
import matplotlib.pyplot as plt
import numpy as np
from scipy.stats import ttest_ind

SR_no_perf_needle = [
    0.8666666667, 0.8166666667, 0.9277777778, 0.85, 0.8055555556,
    0.8388888889, 0.8222222222, 0.9, 0.8111111111, 0.8,
    0.7777777778, 0.8, 0.7777777778, 0.8, 0.9222222222
] #slip ratio without perforation needle

SR_vibrating_needle = [
    0.7444444444, 0.8, 0.8444444444, 0.8, 0.9111111111,
    0.8333333333, 0.8555555556, 0.8, 0.8388888889, 0.7888888889,
    0.7333333333, 0.7777777778, 0.7555555556, 0.8666666667, 0.8166666667
] #slip ratio with vibrating perforation needle

plt.figure(figsize=(8, 6))
plt.boxplot([SR_no_perf_needle, SR_vibrating_needle], labels=["No perforation needle", "Vibrating perforation needle"], patch_artist=True,
            boxprops=dict(facecolor='lightgrey', color='black'),
            medianprops=dict(color='red')
            )
plt.ylim((0.7,1))
plt.ylabel("Slip ratio",fontsize=24)
plt.xticks(fontsize=16)
plt.yticks(fontsize=16)
plt.savefig("results_layered.pdf", format="pdf", bbox_inches="tight")
plt.show()


# Perform an independent t-test
t_stat, p_value = ttest_ind(SR_no_perf_needle, SR_vibrating_needle) #t- and p-values calculated using welch's t test. to be found in the variable explorer
avg1=np.average(SR_no_perf_needle)
avg2=np.average(SR_vibrating_needle)
```